JOURNAL OF GEOPHYSICAL RESEARCH, VOL. 105, NO. C2, PAGES 3425–3450, FEBRUARY 15, 2000

Blending HF radar and model velocities in Monterey Bay through normal mode analysis

B. L. Lipphardt Jr.,[1] A. D. Kirwan Jr.,[1] and C. E. Grosch[2]
Center for Coastal Physical Oceanography, Old Dominion University, Norfolk, Virginia

J. K. Lewis
Ocean Physics Research & Development, Kalaheo, Hawaii

J. D. Paduan
Department of Oceanography, Naval Postgraduate School, Monterey, California

Abstract. Nowcasts of the surface velocity field in Monterey Bay are made for the period August 1–9, 1994, using HF radar observations blended with results from a primitive equation model. A spectral method called normal mode analysis was used. Objective spatial and temporal filtering were performed, and stream function, velocity potential, relative vorticity, and horizontal divergence were calculated over the domain. This type of nowcasting permits global spectral analysis of mode amplitudes, calculation of enstrophy, and additional analyses using tools like empirical orthogonal functions. The nowcasts reported here include open boundary flow information from the numerical model. Nowcasts using no open boundary flow information, however, still provide excellent results for locations within the observation footprint. This method, then, is useful for filtering high-resolution data like HF radar observations, even when open boundary flow information is unavailable. Also, since the nowcast velocity gradient fields were much less noisy than the observations, this may be an effective method for preconditioning high-resolution observation sets for assimilation into a numerical model.

1. Introduction

We analyze the surface currents and related kinematic and dynamic quantities for Monterey Bay for the period August 1–9, 1994. The data for our analysis come from a high-frequency (HF) radar array. This effort extends in several ways the descriptive analysis of *Paduan and Rosenfeld* [1996]. That study focused on low-frequency motions (2–30 day periods) and a comparison of results between April to September 1992 and August through December 1994. Significant longshore current reversals strongly correlated with wind were reported. Subsequently, *Paduan and Cook* [1997] discussed characteristics of the semidiurnal tidal and diurnal currents from this data set. The semidiurnal currents were driven predominantly by the M2 (12.4 hour) tidal constituent while the diurnal currents were correlated with winds produced by sea breeze processes.

In contrast, the emphasis here is on smaller-scale kinematic and dynamic processes. Our motivation is the effort by *Lewis et al.* [1998] to assimilate this radar data into an adaption of the *Blumberg and Mellor* [1987] hydrodynamic model configured for Monterey Bay. The model domain extended shoreward from 122.60°W and from 36.40°N to 37.15°N, well beyond the radar footprint. A substantial portion of the model domain boundary was open. Tidal heights on the open boundaries were specified from the global tidal model of *Schwiderski* [1981, 1983], and open boundary velocities were specified from the linearized equations of motion.

Although model simulations that assimilated the radar observations produced currents that were in general agreement with the pattern seen in the radar data, *Lewis et al.* [1998] expressed concern that errors in the radar data could cause problems in the simulations. Horizontal divergences calculated from the radar data showed unrealistically large magnitudes, changes in sign from time step to time step, and little coherence between adjacent grid cells. These horizontal divergence patterns, when assimilated into the model, would tend to produce unrealistic sea level differences of the order of meters at adjacent grid cells separated by 2.8 km. *Lewis et al.* [1998] concluded that additional processing of the radar data would be useful in order to minimize such effects. This issue is one of the subjects of this paper.

The experiences of *Lewis et al.* [1998] are likely to be repeated by other coastal zone modelers. This is because in recent years there has been a dramatic increase in the capability to provide high-resolution space and time data of estuarine and coastal regions. HF radar data are but one example. Others are synthetic aperture radars, Lagrangian drifters, new generation passive remote-sensing platforms, and a variety of towed instrumentation suites that provide fine-scale information on the density and velocity fields along ship tracks. These developments have been matched by equally dramatic increases in computational capabilities. Consequently, oceanographers now routinely access both observational and computational capabilities unimagined even a few years ago.

[1]Now at College of Marine Studies, University of Delaware, Newark.
[2]Also at Department of Computer Science, Old Dominion University, Norfolk, Virginia.

Paper number 1999JC900295.
0148-0227/00/1999JC900295$09.00

As demonstrated by the *Lewis et al.* [1998] study, analysis of high-resolution disparate (HRD) data raises many issues not encountered with more traditional oceanographic analyses. Some important issues are the following: (1) The horizontal resolution of HRD data sets may be as fine as, or finer than that of numerical models. Thus these data may contain information about intermittent subgrid-scale processes which would likely be smoothed out by traditional analyses. (2) HRD data sets may not cover the domain of interest uniformly. What roles can other data sources, including historical observations and numerical models, play in filling these spatial voids? (3) In nearshore and estuarine regions the domain boundaries may have large open flow segments. How can one blend coarse-scale information from models and historical databases on open boundaries with HRD data from the domain interior to produce reliable nowcasts? (4) HRD data sets have different accuracies, temporal and spatial resolutions, and spatial footprints. How can such highly variable data be blended with numerical model results to produce useful nowcasts?

Here we illustrate these problems using the HF radar data and show one way that they can be addressed. We begin with the premise that nowcasts should incorporate as many dynamics as possible. This study uses a primitive equation model to specify time-dependent open boundary velocities and a few randomly selected interior values. However, other data sources would have been used if they were available. It is not reasonable to expect any single approach to address all of the above concerns optimally.

We stress that the methodology used here is not critically dependent on the availability of open boundary flow information. In fact, if such information is not used, the approach still provides useful nowcast velocities at locations where the observations are made. This closed-boundary nowcast smooths errors inherent in the observations, is three-dimensionally incompressible, and ensures no normal flow at the coastline. The closed-boundary nowcast would be useful, then, for filtering HF radar observations prior to additional analyses. However, this type of closed-boundary nowcast would not be useful for estimating velocities at locations within the nowcast domain where no observations are available. Statistically based inverse methods could be used to fill these spatial gaps. This approach is not explored here. However, our limited experience suggests that the closed-boundary nowcast would be an effective method for preconditioning the observations prior to application of an inverse technique.

For the more general problem considered here, we see two critical problems. One is how to fill spatial voids when the HRD data set does not cover the nowcast domain uniformly. Some combination of historical data, other observations, and model results must be used, and some weighting is appropriate as none of these data sources will necessarily be in dynamic balance with the HRD data. The second problem is how to properly constrain the nowcast at the domain open boundaries. Whatever scheme is employed should result in no normal flow at impermeable boundaries and the specified normal flow through open boundaries.

These two problems are best addressed with a spectral approach rather than through local interpolation and extrapolation. Most spectral approaches do not impose a significant computational penalty compared to local methods. Moreover, all spectral approaches should converge to the same (but not necessarily correct) result if enough terms are retained. Additionally, the mathematical structure of spectral methods makes them ideally suited for filtering independently in space and time.

Here we use a generalization of a spectral method first described by *Rao and Schwab* [1981] in an analysis of currents in Lake Ontario. More recently, this method has been applied to drifter and model data from the Black Sea [*Eremeev et al.*, 1992a, b], cesium contamination in the Black Sea from the Chernobyl incident [*Eremeev et al.*, 1995a, b], HF radar data [*Lipphardt et al.*, 1997], and moored current meter data on the Texas-Louisiana shelf [*Cho et al.*, 1998].

Rao and Schwab [1981] described their method as one form of objective analysis. *Cho et al.* [1998] describe their approach as a two-dimensional Fourier analysis, since they use an orthonormal, boundary-fitted coordinate system. Since our basis functions are calculated on a Cartesian grid and depend only on the geometry and resolution of the nowcast domain (with no dependence on observations or boundary conditions), we will refer to our spectral method as normal mode analysis (NMA). This method has several desirable attributes: (1) Any number of disparate observation data sets can be incorporated into the nowcast. (2) Specified normal flow at open boundaries and no normal flow through closed boundaries are exactly matched in the resulting nowcast. (3) Since the spatial resolution of the NMA basis functions is unconstrained, disparate data sources with different spatial resolutions can be easily combined. (4) The nowcast velocity field is automatically three-dimensionally incompressible. (5) Objective, independent spatial and temporal filtering of the disparate data is readily accomplished. (6) Stream function, velocity potential, and velocity gradient fields such as horizontal divergence and relative vorticity are easily recovered to the same order of accuracy as the nowcast velocity field. (7) The basis functions permit natural partitioning of the nowcast field into separate vorticity and divergence components. (8) Objective analysis (OA) methods, such as those discussed by *Davis* [1985], can be readily incorporated into the NMA methodology. In the present study, the nowcast fields agree with the data to within reasonable estimates of the observational error. As a result, we have not employed OA methods here.

Section 2 describes the data used for the nowcasts. Section 3 discusses the analysis of the velocity field for Monterey Bay. Section 4 addresses the important issues of temporal and spatial filtering using this approach. Section 5 discusses the nowcast results. Section 6 presents a brief summary and discusses the limitations of the approach.

2. Sources of Velocity Data for the Nowcast

The velocity nowcasts made here rely primarily on measurements of near-surface current velocities in Monterey Bay from a Coastal Ocean Dynamics Applications Radar (CODAR) HF radar system. Regular velocity measurements, at 2 hour time intervals, were available for the entire month of August 1994. During this period, data were collected and averaged from three radar sites around the Bay perimeter. The processed CODAR data we use come from a uniform grid with a horizontal resolution of 2 km. A detailed description of the CODAR observations and an analysis of the low-frequency motions they describe are given by *Paduan and Rosenfeld* [1996]. Although their data could not be used to report an expected accuracy of CODAR measurements, they did make quantitative comparisons between filtered CODAR observations and ADCP current measurements, reporting rms speed differences

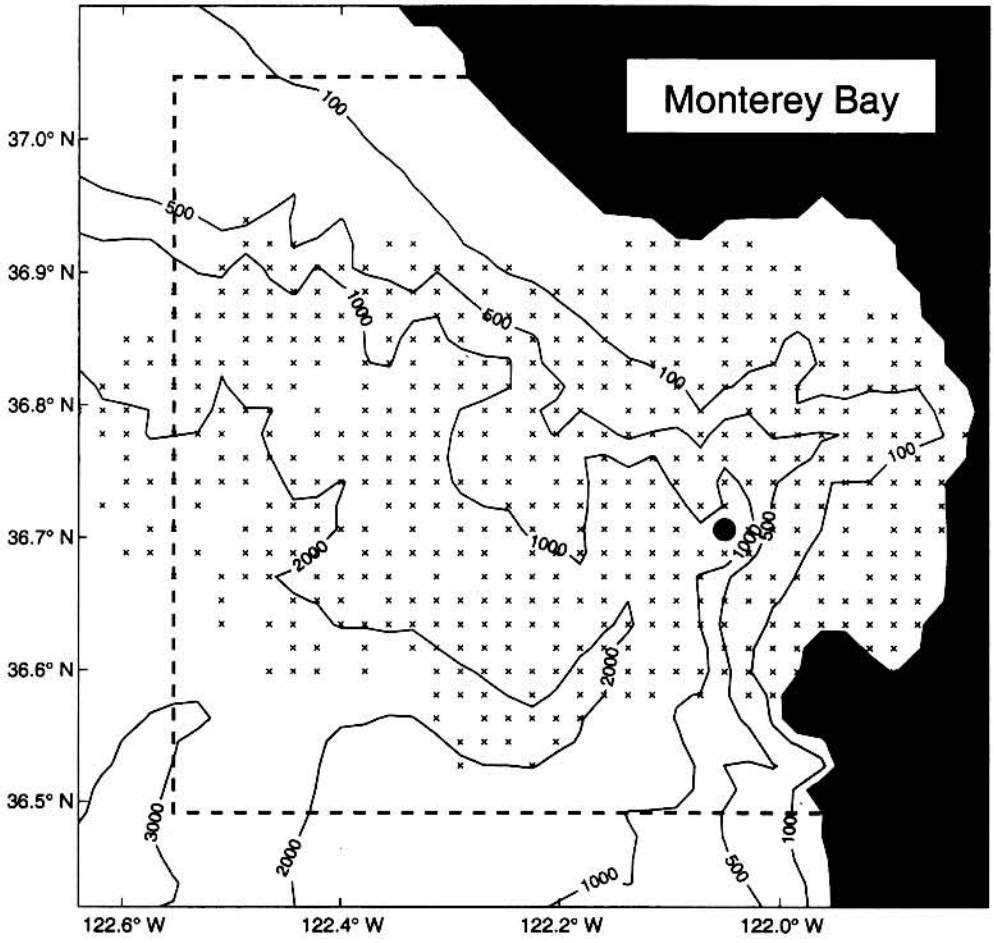

Figure 1. Domain used for surface velocity nowcasting in Monterey Bay. Contours of bottom depth (in meters) are shown. The dashed lines show the open boundaries that define the nowcast region. The crosses show the locations of CODAR velocity measurements for 0100 UT, August 9, 1994. The solid circle near the center shows the location of wind observations used to provide wind forcing for the numerical model.

of 6–11 cm s^{-1} and rms direction differences of ~51°. A more detailed intercomparison of in situ velocity measurements with an HF Ocean Surface Current Radar (OSCR) off Cape Hatteras, North Carolina, reported by *Chapman et al.* [1997] suggests an upper bound on the accuracy of OSCR radial velocities of 7–8 cm s^{-1}.

The CODAR observations by themselves are insufficient to constrain a nowcast on a domain with open boundaries unless the open boundaries lie entirely within the CODAR footprint. In that unlikely case, the CODAR observations can be used to estimate surface currents at the open boundary. Here, however, the nowcast domain extends beyond even the largest CODAR footprint, so that some additional data source is required to specify open boundary flow. We use surface velocity data from the *Lewis et al.* [1998] numerical model to constrain the open boundary flow problem. A map of the model domain, with bottom topography, is shown in Figure 1. Some important features of the *Lewis et al.* [1998] model simulation include the following: (1) At model grid points where CODAR observations were available, these observations were assimilated by the model using an optimized nudging scheme. (2) Wind observations from the Monterey Bay Aquarium Research Institute mooring M1 (marked by a solid circle in Figure 1) were applied to every model grid point as a uniform wind-forcing field. (3) Tidal forcing was used at the model's open boundaries, but no explicit information about larger-scale flows like the California Current was included.

For our analysis the open boundaries that define the nowcast domain (shown as dashed lines in Figure 1) were moved inward by four grid points from the true model boundary to ensure that nowcast boundary velocities will be determined by the model's dynamics and will not be strongly influenced by the model's radiation boundary condition. The crosses shown in Figure 1 show the CODAR observation footprint for 0100 UT, August 9, 1994, as an example of a typical CODAR footprint. The spatial extent and data density of this footprint varied over time; however, these variations are readily accommodated by the NMA analysis. Spatial coverage variability is typical of HRD observations.

CODAR measurements of surface velocity vary in their spatial coverage over time for a variety of reasons discussed by *Paduan and Rosenfeld* [1996]. Although both the size of the radar footprint and the uniformity of data coverage within the footprint show time variations, variations in footprint size are most troublesome. To complicate the spatial coverage problem, the northwest and southwest corners of the nowcast domain extend beyond even the largest available CODAR footprint. Figure 1 shows typical spatial gaps that exist at the

northwest and southwest domain corners, as well as gaps within the footprint. Sources of additional velocity information from within these spatial gap regions will be required to properly constrain the nowcast.

NMA readily accepts any number of disparate sources of velocity observations, fitting spectral amplitudes to the entire observation set in a least squares sense. Consequently, we could look to other data sources such as ADCPs, Lagrangian drifters, current meters, climatology, and numerical models to provide additional velocity observations where spatial gaps exist. If data sets of differing accuracies are available, the least squares approach is readily adapted to include OA techniques [*Davis*, 1985]. For the nowcasts reported here, the *Lewis et al.* [1998] model was randomly sampled in regions where spatial gaps exist in the CODAR data coverage, providing the necessary additional nowcast constraints. Details of how spatial gap regions were identified and how the model was randomly sampled in these regions are discussed in section 3.4.

3. Nowcasting Surface Velocity Using NMA

Nowcasts of surface velocity were made for Monterey Bay at each point on a gridded domain based on the 39 × 39 numerical model grid used by *Lewis et al.* [1998]. The grid has 2 km spacing in both the west-east and south-north directions. Nowcasting was done at 2 hour intervals for the period 0700 UT, August 1, 1994, to 1700 UT, August 9, 1994.

As given by *Eremeev et al.* [1992a], the three-dimensional incompressible velocity field is expressed in terms of two scalar potentials as

$$\vec{u} = \nabla \times [\hat{k}(-\Psi) + \nabla \times (\hat{k}\Phi)]. \tag{1}$$

Here, $\hat{k}$ is the unit vector in the vertical direction. It is important to note that this form ensures that the velocity field is exactly incompressible in three dimensions.

Following traditional methods for the solution of boundary value problems, we begin by partitioning the surface velocity field at each grid point into two components: (1) The homogeneous solution: the velocity field constrained solely by both CODAR and model surface velocities with no flow through the domain boundaries. (2) The inhomogeneous solution: a two-dimensional velocity field due solely to the specified normal flow through the domain's open boundaries.

3.1. Homogeneous Solution

The interior velocity field is represented as an eigenfunction expansion. Since we require both horizontal divergence and relative vorticity for process studies, we choose a basis set consisting of two groups of basis functions, Dirichlet modes and Neumann modes. These basis functions are two-dimensional, representing the surface layer, with an irregular boundary, as shown in Figure 1.

Calculation of these basis functions on a domain with an irregular boundary must be done numerically. Here, we use a FORTRAN library implementation (the ARPACK library) of the Arnoldi method, a direct method for determining eigenvalues of large, sparse matrix systems. All residuals for numerical calculation of the basis functions were $<1.0 \times 10^{-12}$.

As shown by *Eremeev et al.* [1992a], calculation of the vertical component of relative vorticity from (1) in a Cartesian coordinate system gives a Helmholtz equation for Ψ. Here, Ψ is expanded using eigenfunctions which we call Dirichlet modes (ψ_n). They are solutions to

$$\nabla^2\psi_n + \lambda_n\psi_n = 0, \qquad \psi_n|_{\text{boundary}} = 0. \tag{2}$$

The ψ_n may be thought of as a stream function or vorticity mode, with zero horizontal divergence. From (1) the gradients of ψ_n are expressed as

$$(u_n^D,\ v_n^D) = \left(\frac{-\partial\psi_n}{\partial y},\ \frac{\partial\psi_n}{\partial x}\right). \tag{3}$$

As given by *Eremeev et al.* [1992a], calculation of the vertical velocity component from (1) in a Cartesian coordinate system gives a Helmholtz equation for Φ. Here, Φ is expanded using eigenfunctions which we call Neumann modes (ϕ_m). They are solutions to

$$\nabla^2\phi_m + \mu_m\phi_m = 0, \qquad (\hat{k}\cdot\nabla\phi_m)|_{\text{boundary}} = 0. \tag{4}$$

The ϕ_m may be thought of as a velocity potential or divergence mode, with zero relative vorticity. From (1) the gradients of ϕ_m are expressed as

$$(u_m^N,\ v_m^N) = \left(\frac{\partial\phi_m}{\partial x},\ \frac{\partial\phi_m}{\partial y}\right). \tag{5}$$

3.2. Inhomogeneous Solution

The homogeneous solutions satisfy zero normal flow at all boundaries. This is appropriate for impermeable boundaries like the coastline but is not appropriate for open boundaries where there will generally be both normal and tangential flow. Information about the flow at open boundaries can be included in the nowcast through the use of an inhomogeneous solution, which can be constructed to account for either the normal or tangential open boundary flow but not both.

To account for the normal component of the flow at the domain's open boundaries, a boundary velocity potential solution Θ can be calculated numerically at each nowcast time as the solution to

$$\nabla^2\Theta(x, y, 0, t) = S_\Theta(t), \qquad (\hat{n}\cdot\nabla\Theta)|_{\text{boundary}} = (\hat{n}\cdot\vec{u}_{\text{model}})|_{\text{boundary}},$$

where $\hat{n}$ is the unit outward normal vector on the boundary, $\vec{u}_{\text{model}}$ is surface velocity from the *Lewis et al.* [1998] model, and S_Θ is a source term that accounts for the net flow into the domain through its open boundaries (tidal effects). S_Θ is defined as

$$S_\Theta(t) = \frac{\oint \hat{n}\cdot\vec{u}_{\text{model}}\, dl}{\iint dx\, dy}.$$

To account for the tangential component of the flow at the open boundaries, a boundary stream function Υ can be calculated numerically at each nowcast time as the solution to

$$\nabla^2\Upsilon(x, y, 0, t) = S_\Upsilon(t), \qquad \hat{t}\cdot[\nabla\times(-\hat{k}\Upsilon)]|_{\text{boundary}} = (\hat{t}\cdot\vec{u}_{\text{model}})|_{\text{boundary}},$$

where $\hat{t}$ is the unit tangent vector on the boundary, taken in the positive sense, and S_Υ is a source term that accounts for the net circulation on the domain boundary. S_Υ is defined as

$$S_Y(t) = \frac{\oint \hat{t} \cdot \tilde{u}_{\text{model}}\, dl}{\iint dx\, dy}.$$

It is important to stress that the inhomogeneous solution cannot account for both the normal and tangential boundary flow components simultaneously, as this would be equivalent to an overspecification of (1). Thus an a priori decision must be made as to whether specification of the normal or tangential boundary flow component is most appropriate.

Here, we have elected to use the inhomogeneous solution to specify the normal component of open boundary flow. This seems appropriate, since the boundary information comes from a tidally forced model. We stress that we do not suggest this approach as a universal paradigm. Other nowcast problems will undoubtedly require different strategies for dealing with open boundary flow.

Numerical solutions for Θ were determined using a double-precision version of the generalized minimum residual method for sparse matrices included in the SPARSKIT FORTRAN library, with residuals always $<1.0 \times 10^{-11}$. From Θ, finite difference inhomogeneous solution velocities were calculated as

$$(u^i, v^i) = \nabla\Theta(x, y, 0, t). \tag{6}$$

Contour plots of Θ and vector plots of the associated velocity field are shown for 0100 UT and 1300 UT on August 9, 1994, in Figure 2. Spectral analysis of the open boundary velocities shows a dominant peak at the diurnal frequency. This was expected, since *Lewis et al.* [1998] used a combination of diurnal and semidiurnal tidal forcing along the model's open boundary and the wind forcing contains strong diurnal fluctuations. The times shown in Figure 2 were chosen to represent two tidal extremes in the boundary velocity flow field.

Note that the Θ and velocity fields shown in Figure 2 are constrained only by the model normal surface velocities on the nowcast open boundary and the requirement for no normal flow across the closed domain boundaries. These fields represent that portion of the total velocity field that is due to normal flow at the open boundaries.

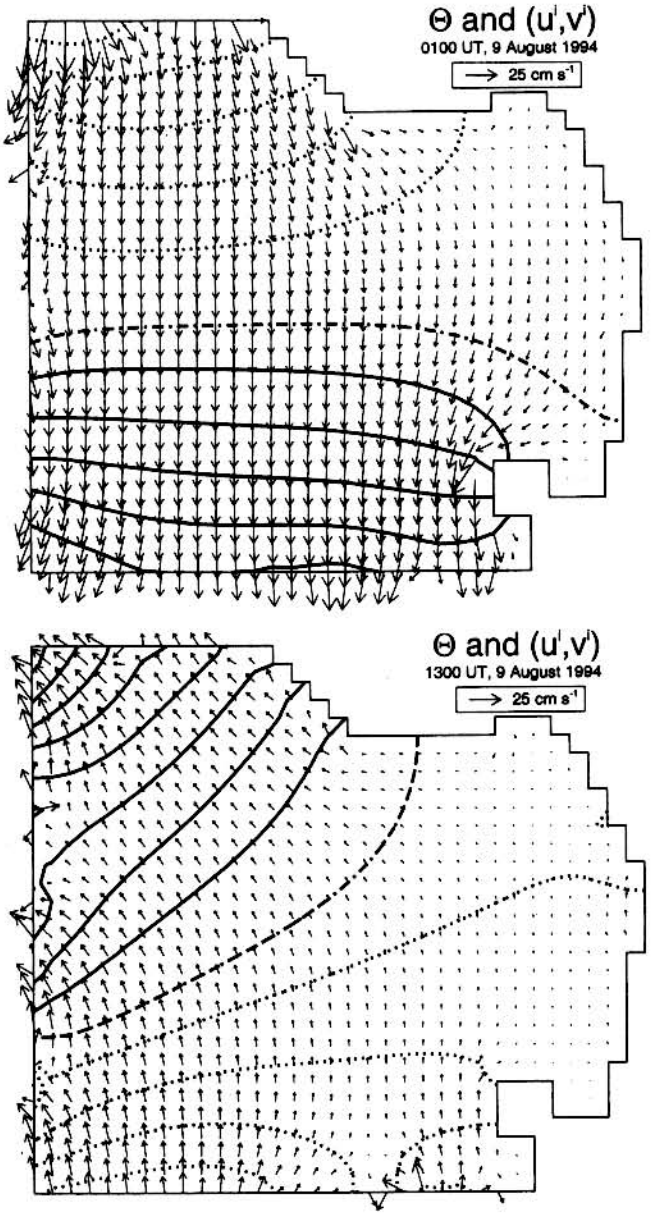

Figure 2. Contour plots of Θ (nondimensional) with velocity vectors (in cm s^{-1}) overlaid for 0100 UT and 1300 UT on August 9, 1994. Positive values are shown as solid contours. Negative values are shown as dotted contours. The zero contour is dash-dotted.

3.3. Complete NMA Nowcast

For the domain shown in Figure 1, 50 ψ_n and 50 ϕ_m modes were determined numerically. When the spectral representation for the interior velocity solution is combined with the boundary velocity field derived from Θ, the horizontal surface velocity components are expressed as

$$u(x, y, 0, t) = \sum_{n=1}^{N} \frac{A_n(0, t)}{\gamma_n^D} u_n^D(x, y) + \sum_{m=1}^{M} \frac{B_m(0, t)}{\gamma_m^N} u_m^N(x, y) + u^i(x, y, 0, t), \tag{7a}$$

$$v(x, y, 0, t) = \sum_{n=1}^{N} \frac{A_n(0, t)}{\gamma_n^D} v_n^D(x, y) + \sum_{m=1}^{M} \frac{B_m(0, t)}{\gamma_m^N} v_m^N(x, y) + v^i(x, y, 0, t), \tag{7b}$$

where (u^i, v^i) are the inhomogeneous velocity components shown in (6), (u_n^D, v_n^D) are the Dirichlet mode velocities shown in (3), (u_m^N, v_m^N) are the Neumann mode velocities shown in (5), and

$$\gamma_n^D = \frac{\iint [(u_n^D)^2 + (v_n^D)^2]\, dx\, dy}{\iint dx\, dy},$$

$$\gamma_m^N = \frac{\iint [(u_m^N)^2 + (v_m^N)^2]\, dx\, dy}{\iint dx\, dy},$$

so that $(A_n/\gamma_n^D)^2$ and $(B_m/\gamma_m^N)^2$ are proportional to kinetic energy. This normalization allows for comparison of mode kinetic energies, which is useful as a criterion for spatial filtering.

From (1), if u and v are known in two horizontal layers, the mean vertical velocity between the layers is expressed as

$$w(x, y, z, t) = -\sum_{m=1}^{M} \tilde{B}_m(z, t)\left[\frac{\partial^2\phi_m(x, y)}{\partial x^2} + \frac{\partial^2\phi_m(x, y)}{\partial y^2}\right],$$

$$\tilde{B}_m(z, t) = \int^z B_m(z', t)\, dz'.$$

We include the above w equation for completeness, but since we analyze only the surface velocity field, we are unable to estimate w here.

The A_n and B_m amplitudes above are determined by minimizing the following error measure:

$$\sigma^2 = \frac{1}{K}\sum_{k=1}^{K} W_k^u(\tilde{u}_k - u_k^h)^2 + \frac{1}{L}\sum_{l=1}^{L} W_l^v(\tilde{v}_l - v_l^h)^2,$$

$$(\tilde{u}, \tilde{v}) = (u^{\text{obs}}, v^{\text{obs}}) - (u^i, v^i),$$

$$(u^h, v^h) = (u, v) - (u^i, v^i).$$

Here $(u^{\text{obs}}, v^{\text{obs}})$ are measured velocities, either from CODAR observations or model data sampled from the interior. K and L are the total number of u^{obs} and v^{obs}, respectively. From (4), (u, v) are nowcast velocities. Weighting factors (W^u, W^v) might be used to account for statistical correlations in the observations, using methods similar to those described by *Davis* [1985]. Here, since the CODAR velocities are reported on a uniformly spaced grid and we make no assumptions about their statistical properties, (W^u, W^v) are set to 1.0, so that our results represent the simplest implementation: a uniformly weighted, linear least squares minimization.

Typically, 500–600 measured velocities (1000–1200 velocity component equations) were used to determine up to 50 A_n and 50 B_m amplitudes, so that the linear system was always overdetermined. The linear least squares minimization problem was solved numerically using a FORTRAN implementation of the QR (orthogonal–upper triangular) matrix factorization technique provided in the LAPACK library.

From (7), to the same order of accuracy as u and v, stream function Ψ, velocity potential Φ, relative vorticity ς, and horizontal divergence $(\nabla_H \cdot \vec{u})$ are expressed as

$$\Psi(x, y, 0, t) = \sum_{n=1}^{N} A_n(0, t)\psi_n(x, y), \tag{8}$$

$$\Phi(x, y, 0, t) = \sum_{m=1}^{M} B_m(0, t)\phi_m(x, y) + \Theta(x, y, 0, t), \tag{9}$$

$$\varsigma = \hat{k} \cdot \nabla \times \vec{u}(x, y, 0, t) = -\sum_{n=1}^{N} A_n(0, t)\ \lambda_n\psi_n(x, y), \tag{10}$$

$$\nabla_H \cdot \vec{u}(x, y, 0, t) = -\sum_{m=1}^{M} B_m(0, t)\mu_m\phi_m(x, y), \tag{11}$$

where $\nabla_H = (\partial/\partial x, \partial/\partial y)$. Note that the above expressions for ς and horizontal divergence do not require differentiation of the ψ_n or ϕ_m fields.

3.4. Spatial Gaps

Early in our work, we attempted to use 100 modes to combine CODAR observations with open boundary flow information from the model, with no information about flow in the large spatial gap regions in the northwest and southern portions of the domain (see Figure 1). That nowcast produced large unrealistic flows in the spatial gap regions. We identified two possible approaches to eliminating these regions of large, unrealistic flow. One approach would be to simply reduce the total number of nowcast modes used. As the mode set is reduced, the smallest spatial scale resolved by the mode set increases. When the smallest resolved spatial scale becomes larger than the spatial scale of the gaps, the spurious unrealistic flow problem vanishes. However, using this approach for domains with large spatial gaps will sharply reduce the spatial resolution of the nowcast.

A second approach would be to supplement the CODAR observations with velocity information for the spatial gap regions from another source. Since we wish to demonstrate how the NMA method can be used to blend disparate data sources, we have chosen the second approach to solving the spatial gap problem: We supplement the CODAR observations with model surface velocities randomly sampled from the spatial gap regions. All CODAR measurements inside the domain were included in the nowcast. Spatial gap points on the nowcast grid were identified as any interior grid point with no available CODAR measurement inside a 2 km radius circle centered on the point. To fill these spatial gaps, the group of spatial gap points was randomly sampled, and both the u and v model velocity components at each sampled gap point were then added to the set of measured velocities.

To determine the minimum amount of supplemental model data needed to fill the spatial gaps, a series of nowcasts were made using various sizes of randomly sampled model velocity populations. Comparison of these nowcasts showed that no more than ~20% sampling was needed in the spatial gap regions and that the nowcast was insensitive to increases in this model sample population size. As a result, we report results only for nowcasts using an approximate 20% sampling rate.

Figure 3 shows the number of CODAR (solid line) and model (dashed line) velocity components used to constrain the nowcast at each time. Figure 4 shows distributions of measured velocities used for two nowcasts. The upper plot (0700 UT,

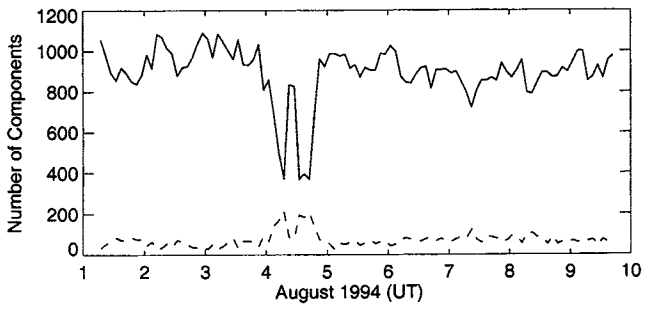

Figure 3. Number of CODAR (solid line) and model (dashed line) velocity components used to constrain the 100-mode nowcast at each time.

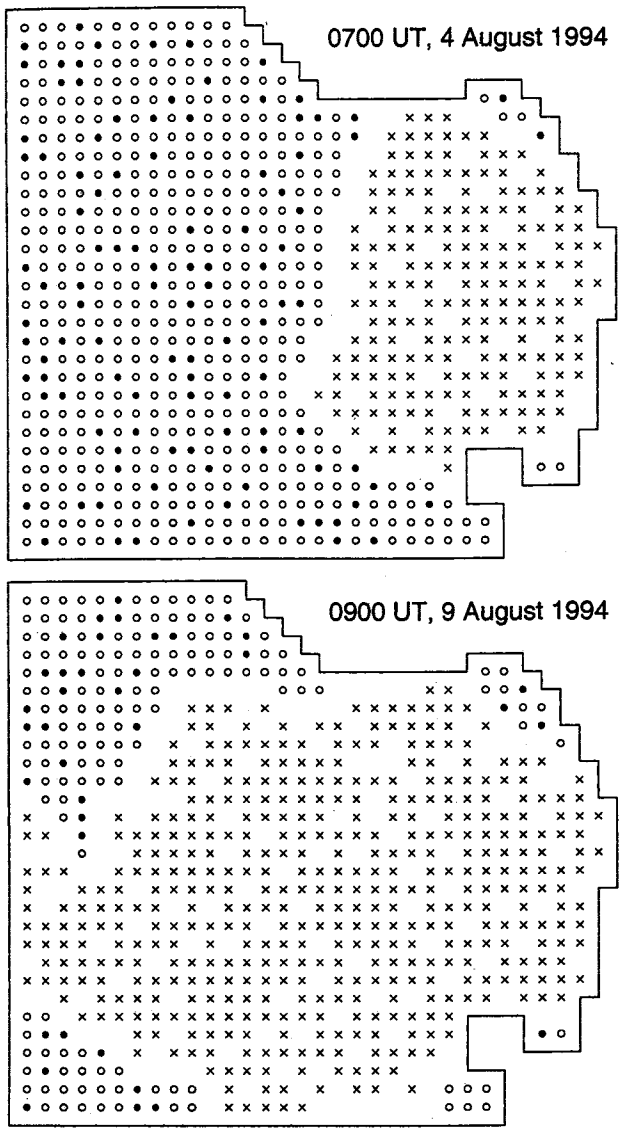

Figure 4. Distribution of measured velocities used for two nowcasts. CODAR observations are shown as crosses. Locations which meet our criterion for a spatial gap are shown as circles, with solid circles indicating those spatial gap points where randomly sampled model velocities were used as additional measured velocities. Blank spaces in the grid show locations where no CODAR observations were available and where our spatial gap criterion was not met.

August 4, 1994) shows a case with a very small CODAR footprint, so that the population of sampled interior model points is large. The lower plot (0900 UT, August 9, 1994) shows a case where the CODAR footprint was quite large, covering most of the nowcast domain.

3.5. Summary of the Nowcast Method

To summarize, the important steps of the NMA nowcast are as follows: (1) Compute Dirichlet (ψ_n) and Neumann (ϕ_m) basis functions and their gradients numerically for the nowcast domain. This only needs to be done once, since the basis functions are not time dependent. (2) At each nowcast time, compute the inhomogeneous velocity field (u^i, v^i) using the best available information about normal flow through the nowcast domain open boundaries. (3) At each nowcast time, compute the mode amplitudes (A_n, B_m) for the homogeneous velocity field as the least squares fit to all available disparate velocity observations. (4) Temporally filter the (A_n, B_m) time series, if desired. (5) At each nowcast time, use (7)–(11) to calculate velocity components and other kinematic or dynamic quantities at each point on the nowcast grid.

4. Using NMA for Objective Filtering

The spectral nature of the NMA approach allows for separate temporal and spatial filtering in an objective way. For spatial filtering, the complete 100-mode nowcast serves as a basis for selecting a reduced mode set. Since the basis functions are normalized, mode selection is based on comparison of properties of the mode amplitudes. It is important to note that the form of the mode amplitude used for comparison depends on which kinematic or dynamic quantity is to be analyzed. Table 1 shows the particular amplitude forms most useful for spatial filtering as part of the NMA analysis of the nowcast quantities defined in (7)–(11).

A variety of different schemes might be considered for spatial filtering, based on various properties of the mode amplitudes. A few examples of possible spatial filtering schemes are the following: (1) Calculate a representative value for each mode amplitude time series (rms, mean-square, etc.) and retain only those modes with values greater than a specified threshold. (2) Examine the power spectra for each mode amplitude time series and retain only those modes that have at least one statistically significant spectral peak. (3) Examine the spatial scales resolved by each mode basis function and retain only those modes that resolve spatial scales in a specified range.

Here we focus on analysis of the velocity field, and we use a spatial filtering scheme based on the kinetic energy contained in each mode. Our spatial filtering scheme is described in section 4.1.

Many other spatial filtering mode selection schemes could also be devised. It is not possible to devise a scheme that optimizes the analysis of all quantities defined in (7)–(11) simultaneously. Spatially filtered nowcasts of the velocity and relative vorticity fields, for example, will almost certainly use different subsets of the full 100-mode basis set, depending on how the mode selection criteria are developed.

When the reduced mode set has been selected through spatial filtering, the time series of each mode amplitude can be temporally filtered, if desired. Many temporal filtering schemes are possible. Our temporal filtering scheme will be described in section 4.2.

Table 1. Mode Amplitude Forms Most Useful for Mode Selection During Spatial Filtering

Field To Be Analyzed	Amplitude Form
Ψ	A_n
Φ	B_m
(u, v)	A_n/γ_n^D and B_m/γ_m^N
$\hat{k} \cdot \nabla \times \vec{u}$	$-\lambda_n A_n$
$\nabla_H \cdot \vec{u}$	$-\mu_m B_m$

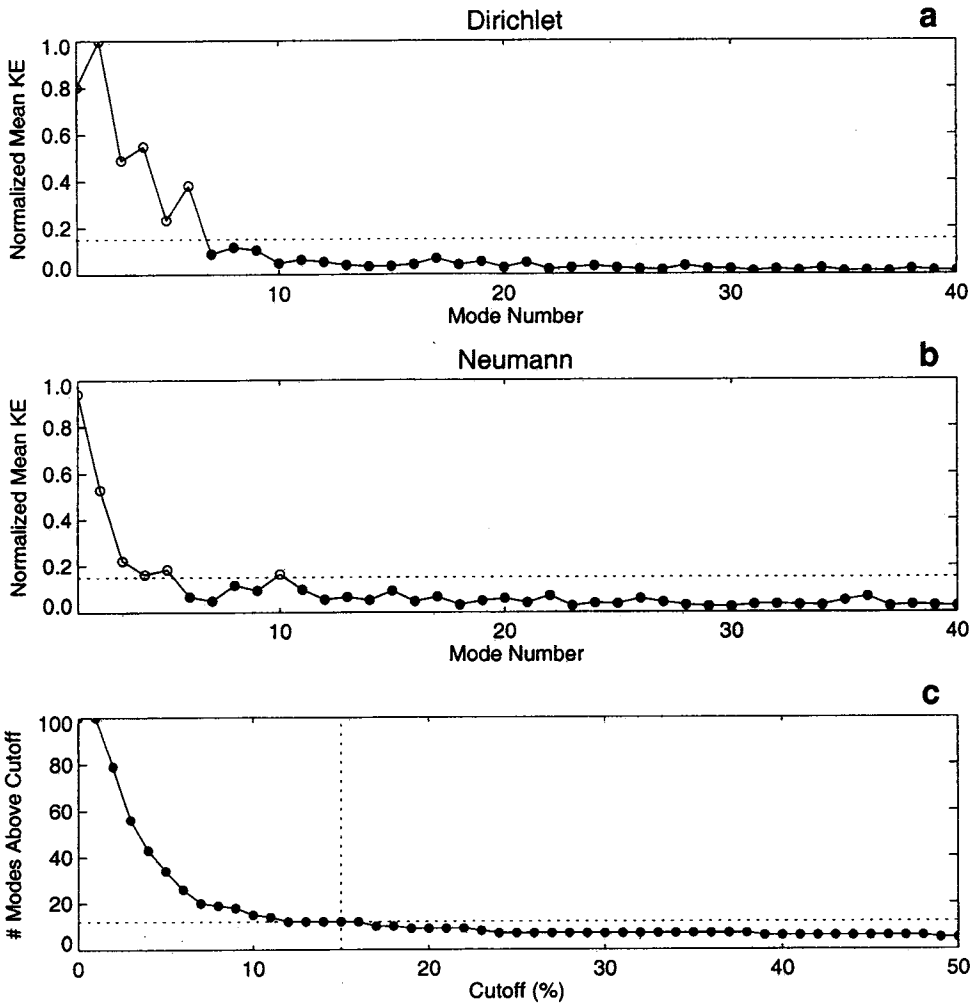

Figure 5. (a) Normalized mean A_n kinetic energy $\overline{\text{KE}}$ versus Dirichlet mode number; (b) normalized mean B_m kinetic energy versus Neumann mode number; (c) number of modes retained versus cutoff percentage. The dashed horizontal line in Figures 5a and 5b shows the cutoff value of 15% used to obtain the reduced set of 12 modes.

4.1. Spatial Filtering

Our nowcast analysis focuses primarily on the velocity field, so that, as shown in Table 1, we analyzed $(A_n/\gamma_n^D, B_m/\gamma_m^N)$ to develop a criterion for selecting the reduced mode set. Our criterion was based on the mean kinetic energy $\overline{\text{KE}}$ for each amplitude time series, defined as

$$\overline{\text{KE}}_n^D = \frac{1}{2J}\sum_{j=1}^{J}[A_n(j)/\gamma_n^D]^2,$$

$$\overline{\text{KE}}_m^N = \frac{1}{2J}\sum_{j=1}^{J}[B_m(j)/\gamma_m^N]^2,$$

where J is the number of time intervals in the time series. Here, J is 102.

Note that since the mode velocity fields are normalized and nondimensional, $(A_n/\gamma_n^D, B_m/\gamma_m^N)$ have units of cm s^{-1} so that the square of these amplitudes is proportional to kinetic energy. Our spatial filtering criterion was to retain only those modes with 15% or more of the maximum $\overline{\text{KE}}$ from the 100-mode nowcast. Spatial filtering resulted in a reduced set of 12 total (6 Dirichlet and 6 Neumann) modes.

Figure 5 shows a summary of the spatial filtering procedure. Figure 5a shows a plot of $\overline{\text{KE}}_n^D$ (normalized by the maximum $\overline{\text{KE}}$ value, $\overline{\text{KE}}_2^D$) versus mode number for the 50 Dirichlet modes. Figure 5b shows a plot of $\overline{\text{KE}}_m^N$ (again normalized by $\overline{\text{KE}}_2^D$) for the 50 B_m (Neumann) modes. In Figures 5a and 5b, open circles show values above the 15% cutoff, and solid circles represent values below this cutoff. Figure 5c shows the number of modes that are retained versus cutoff percentage. Cutoff percentage is defined as the ratio of $\overline{\text{KE}}_m^D$ or $\overline{\text{KE}}_m^N$ to the maximum $\overline{\text{KE}}$ value. Any mode that meets or exceeds the cutoff is retained.

Figure 6 shows maps of the six Dirichlet modes ψ_n retained for the spatially filtered nowcast. Figure 7 shows nondimensional vectors representing the gradients of these Dirichlet modes (u_n^D, v_n^D) used in the homogeneous part of the nowcast field as shown in (7). Figures 8 and 9 show similar results for the six Neumann modes used for the spatially filtered nowcast.

As seen in Figure 5a, ψ_1 through ψ_4 are the most energetic Dirichlet modes, and ψ_2 is the dominant mode. Figures 6 and

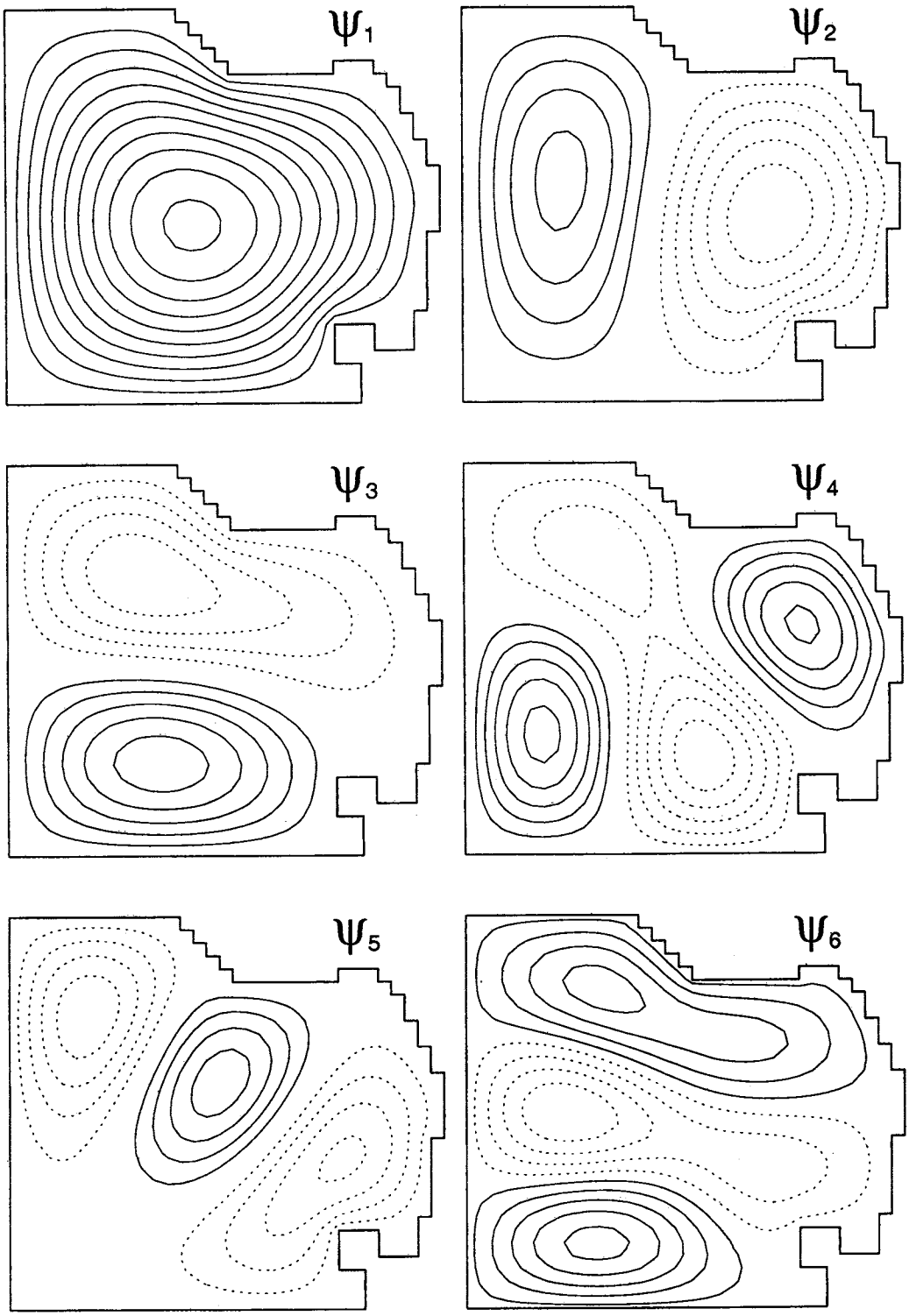

Figure 6. The six Dirichlet modes ψ_n retained for the spatially filtered surface velocity nowcast. Each field has been normalized and is nondimensional. Positive values are shown as solid contours, and negative values are shown as dashed contours.

7 show that a linear combination of ψ_1 and ψ_2 will produce an asymmetrical vortex pair consisting of a large offshore gyre and a smaller oppositely rotating gyre near the coast, consistent with the daily and monthly mean CODAR velocity fields reported by *Paduan and Rosenfeld* [1996]. Figure 5b shows that ϕ_1 and ϕ_2 are the most energetic Neumann modes. From Figures 8 and 9 it can be seen that a linear combination of these modes describes the broad cross-shelf surface layer response to the combined effects of wind and tides.

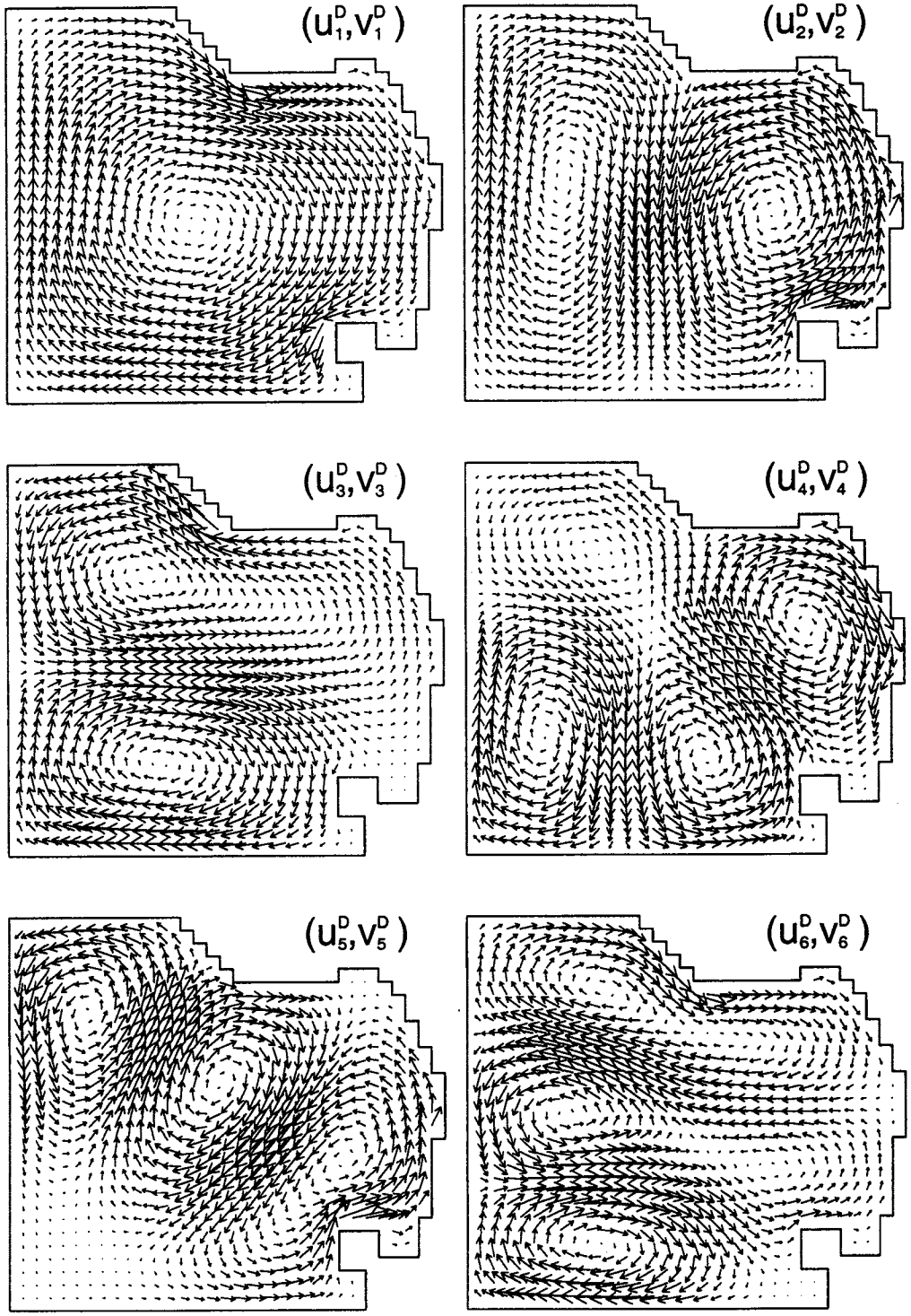

Figure 7. Nondimensional vectors showing the gradients of the six Dirichlet modes (u_n^D, v_n^D) retained for the spatially filtered surface velocity nowcast.

4.2. Temporal Filtering

In general, we expect HRD observations to be irregularly spaced in time; this requires a robust technique like Lomb's method for calculation of power spectra. We use this method here, even though the CODAR observations are uniformly distributed in time. As is well known, Lomb's method spectra are consistent with those obtained using other spectral analysis methods when the time series is uniformly spaced.

The spectra (normalized by the variance of the time series) for the 12 most energetic mode amplitudes (determined during spatial filtering) are shown in Figure 10. The largest peak in each spectrum is marked with a vertical dashed line, and its

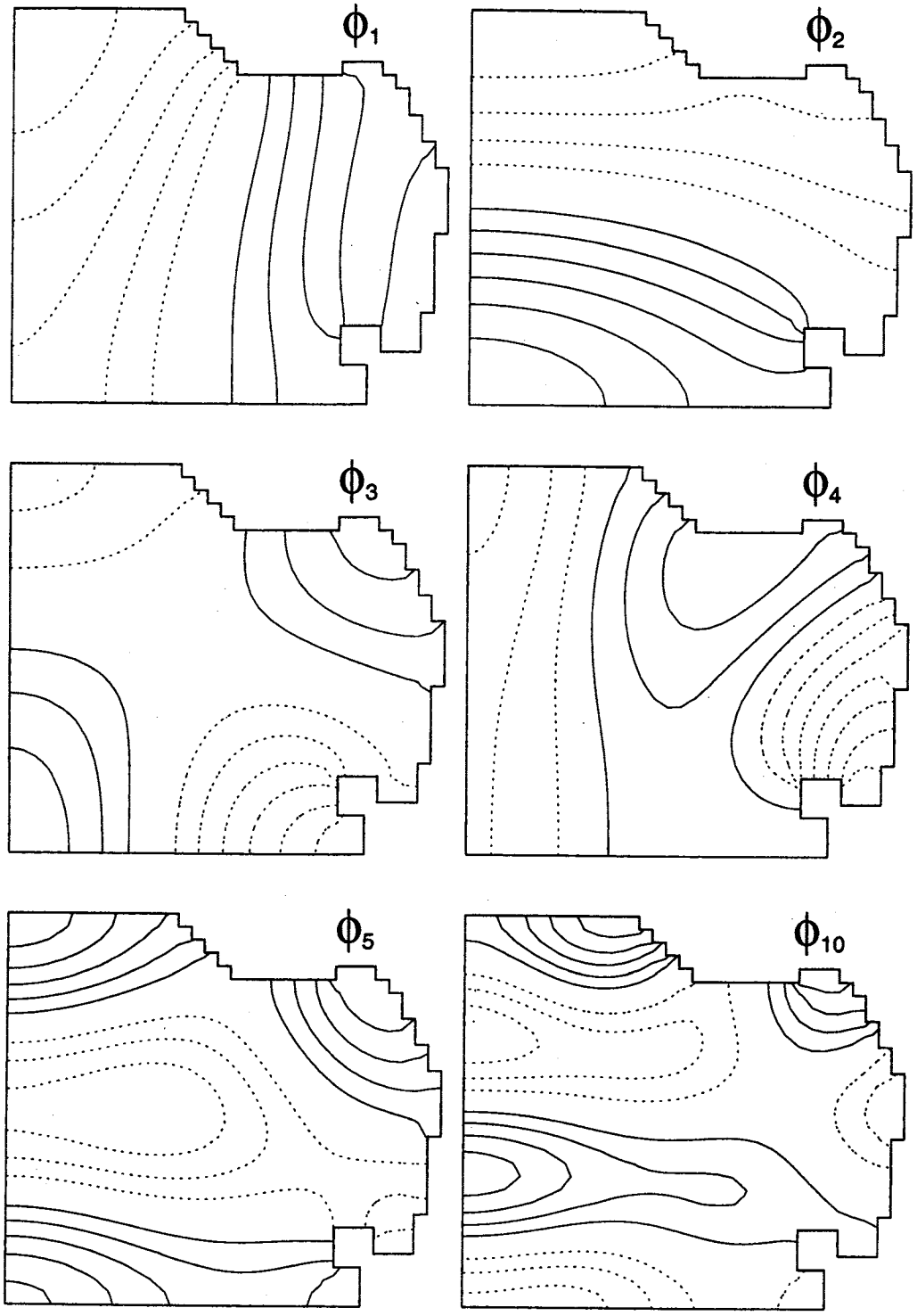

Figure 8. The six Neumann modes ϕ_m retained for the spatially filtered surface velocity nowcast. Each field has been normalized and is nondimensional, with contours presented as in Figure 6.

period is shown at the upper right in each plot, in days. The horizontal dashed lines on each plot indicate probability of significance levels of 95% (upper lines) and 5% (lower lines). These spectra show that except for A_3 and A_6 all of the modes are dominated by oscillations at diurnal and near-diurnal frequencies, consistent with the results reported by *Paduan and Rosenfeld* [1996], who note that the largest signals present at every CODAR observation location derive from tidal period motions that include sea breeze current effects.

For the spatially filtered 12-mode set, temporal filtering was performed by sequentially fitting a quadratic plus three harmonic functions to each amplitude time series. Since the nowcast period spanned only 202 hours, the quadratic fit was used

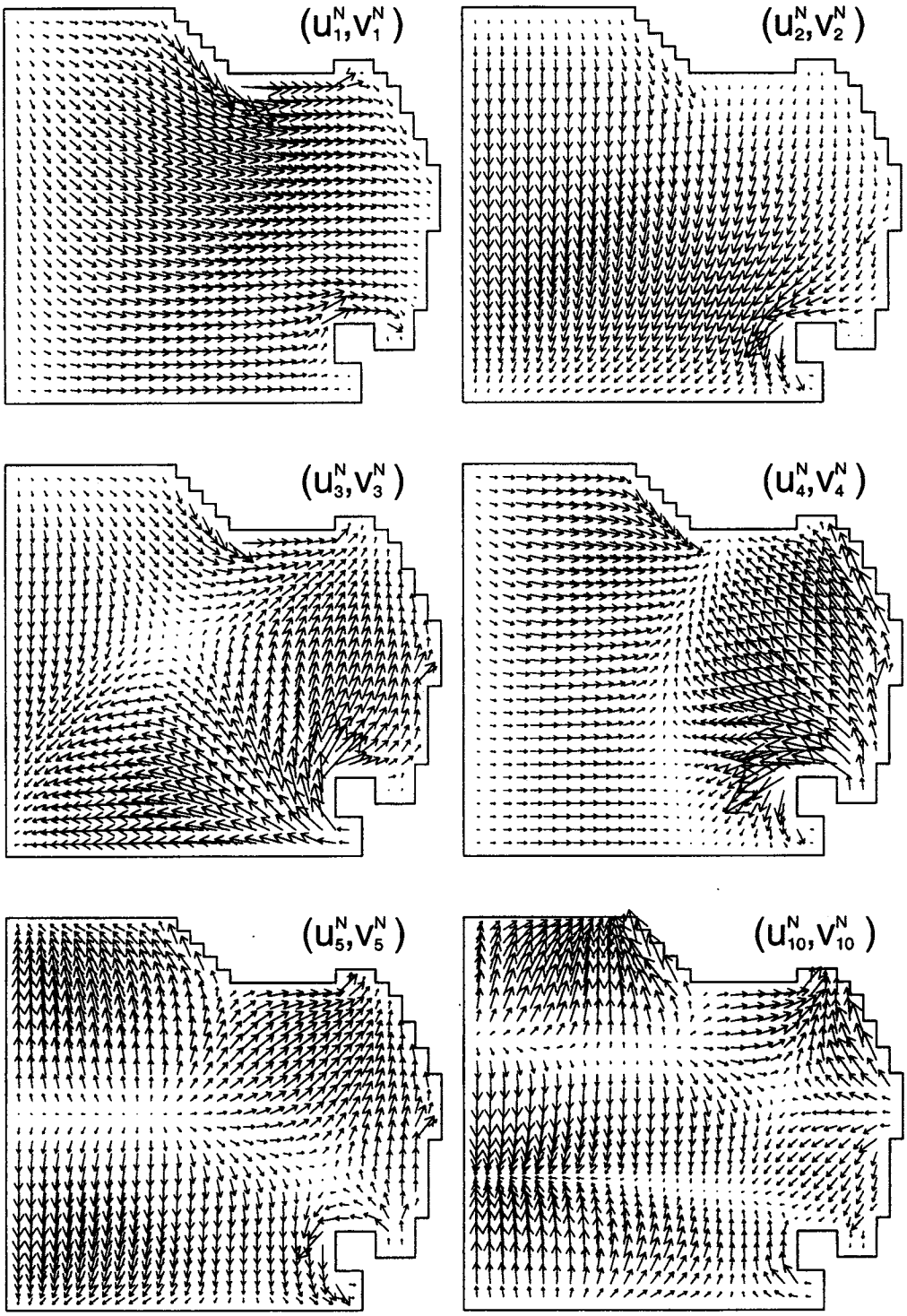

Figure 9. Nondimensional vectors showing the gradients of the six Neumann modes (u_m^N, v_m^N) retained for the spatially filtered surface velocity nowcast.

to account for low-frequency motions (with periods > 10 days) which could not be resolved through spectral analysis. The frequencies for the three harmonic fits were chosen as the frequencies of the three most energetic spectral peaks from spectral analysis of each individual amplitude time series from the 100-mode nowcast. The temporally filtered amplitudes (A_n, B_m), constructed of only the quadratic and three harmonic components, were expressed as

$$A_n(t) = a_n + b_n(t - t_0) + c_n(t - t_0)^2 + \sum_{i=i}^{3} \{d_n^i \cos [\omega_n^i(t - t_0)] + e_n^i \sin [\omega_n^i(t - t_0)]\},$$

$$B_m(t) = a_m + b_m(t - t_0) + c_m(t - t_0)^2 + \sum_{i=i}^{3} \{d_m^i \cos [\omega_m^i(t - t_0)] + e_m^i \sin [\omega_m^i(t - t_0)]\},$$

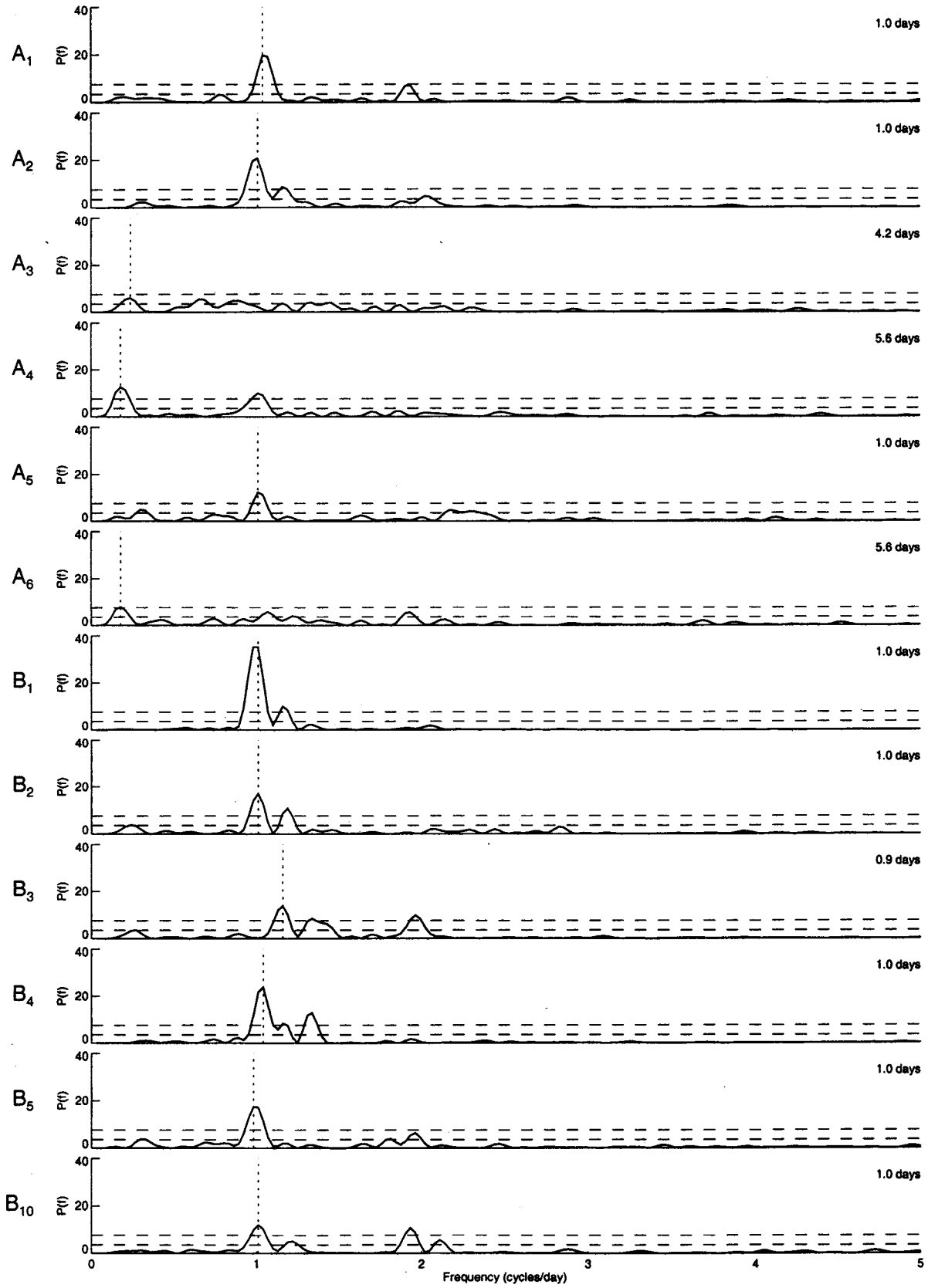

Figure 10. Power spectra for the 12 most energetic mode amplitudes, as determined during spatial filtering. Each spectrum is normalized by the variance of the amplitude's time series. The largest peak in each spectrum is marked with a vertical dashed line, and its period is shown at the upper right in each plot, in days. The horizontal dashed lines indicate probability of significance levels of 95% (upper lines) and 5% (lower lines).

Table 2. Periods of the Harmonics Used to Construct the Temporally Filtered A_n and B_m for the 12-Mode Nowcast

Mode	τ_1	τ_2	τ_3
A_1	0.96	0.52	1.29
A_2	0.99	0.86	0.50
A_3	4.21	1.53	1.12
A_4	5.61	0.99	0.53
A_5	0.99	3.37	0.46
A_6	5.61	0.94	0.52
B_1	0.99	0.86	0.75
B_2	0.99	0.84	4.21
B_3	0.86	0.51	0.75
B_4	0.96	0.75	0.86
B_5	1.02	0.51	0.55
B_{10}	0.99	0.52	0.47

Periods are given in days.

with $n = (1, 2, 3, 4, 5, 6)$ and $m = (1, 2, 3, 4, 5, 10)$. Here, a, b, and c are coefficients of the quadratic fit and d^i and e^i are coefficients of the ith-mode harmonic fit. Table 2 shows the periods for the three harmonics used to temporally filter each mode for the 12-mode nowcast. Figure 11 shows a histogram for the 36 harmonic periods shown in Table 2. Time series of the A_n and B_m used for the 12-mode nowcast are shown as solid lines in Figure 12. The short-dashed lines in Figure 12 show the time series for these amplitudes from the 100-mode nowcast. The long-dashed lines in Figure 12 show the quadratic fit for the 100-mode nowcast time series.

5. Nowcast Results

A comparison of the surface velocity nowcasts using all 100 modes and the reduced set of 12 modes is shown in Figure 13 for 0100 UT, August 9, 1994. Figure 13 shows that both nowcasts generally agree well with the observed CODAR velocities. The 12-mode nowcast (Figure 13c) is smoother, but still describes the larger-scale structure seen in the CODAR data. The spatial smoothing that results from the reduction to a 12-mode set also results in somewhat larger differences with the CODAR observations, as seen in the Figure 13e.

5.1. Vorticity and Divergence

It is difficult to describe the spatial structure of velocity gradient fields like relative vorticity or horizontal divergence using either the CODAR observations or the model surface velocity fields. Spatial and temporal gaps in the CODAR observations prevent finite difference estimation of velocity gradients over the entire domain. Most primitive equation models, including the one used by *Lewis et al.* [1998], calculate the velocity field with a truncation error proportional to δ^2, where δ is the grid spacing. For these models, finite difference estimates of velocity gradients have truncation errors proportional to δ.

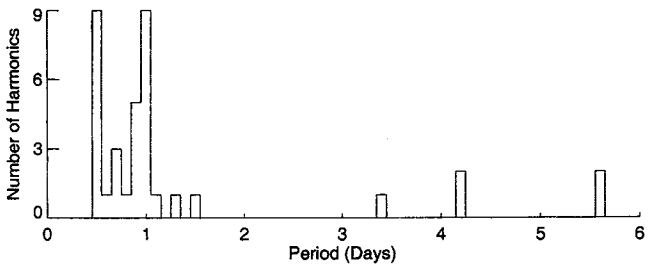

Figure 11. Histogram of the 36 harmonic periods used to construct the temporally filtered A_n and B_m for the 12-mode nowcast.

Figure 14 shows the model velocity, relative vorticity, and horizontal divergence fields for 0100 UT, August 9, 1994. The model relative vorticity and horizontal divergence were calculated using centered finite differences of model velocities. The lack of spatial coherence in the gradient fields reflects the increased truncation error in the finite difference estimates.

Nowcast relative vorticity and horizontal divergence were calculated as in (10) and (11). A comparison of the relative vorticity and horizontal divergence fields for the 100-mode and 12-mode nowcasts is shown in Figure 15 for 0100 UT, August 9, 1994. Figures 15a, 15c, and 15e show the results from the 100-mode case, with the 12-mode results shown in Figures 15b, 15d, and 15f. Comparison of these velocity gradient fields more clearly reveals the underlying spatial filtering: Vorticity and divergence patches in the 100-mode nowcast fields have spatial scales as small as 10 km, while the 12-mode nowcast fields have spatial scales of 20 km or larger. Spatial filtering of the velocity fields results in smoothing of these gradient fields. The nowcast fields shown in Figure 15 can be compared directly to the model results shown in Figure 14, except that the contour interval for the model contour plots in Figure 14 is twice as large as that used in Figure 15.

Figure 15 shows that nowcasting can supplement both the CODAR observations and the model with improved estimates of the spatial structure of the velocity gradient fields. Although the spatial filtering criterion was not based on an analysis of the velocity gradient fields, the kinetic energy–based spatial filtering still clarifies this spatial structure. It is interesting that the 100-mode nowcast vorticity field (Figure 15c) consists of small-scale structures imposed on larger-scale features of the same sign, while the 12-mode nowcast vorticity field (Figure 15d) shows a cyclone inside Monterey Bay, with a companion anticyclone offshore. This pairing of a nearshore cyclone with an offshore anticyclone agrees well with the monthly mean velocity field for August 1994 shown in the lower plot of Figure 12 of *Paduan and Rosenfeld* [1996].

The interpretation of the horizontal divergence structure is not as clear. The 100-mode nowcast divergence shows a ridge of upwelling (divergence) running roughly eastward across the middle of the domain and cutting across the middle of the offshore anticyclone. There is also upwelling along the northern coastline. Some evidence of both of these features is present in the spatially filtered 12-mode horizontal divergence field.

Spatial filtering removes small-scale features in both the relative vorticity and horizontal divergence fields. The underlying large-scale structure in the relative vorticity field is consistent with the large-scale circulation in Monterey Bay. The large-scale structure of the horizontal divergence field is not as easily interpreted.

The NMA nowcast method reduces noise in the nowcast velocity gradient fields in two ways. First, as seen in Figures 5a and 5b, the wave number spectra for Dirichlet and Neumann mode numbers >10 are essentially flat, suggesting that the velocity contributions from these modes contain only white noise. Our technique for spatial filtering eliminates this noise from the 12-mode nowcast. Second, traditional finite difference techniques used to calculate velocity gradients amplify

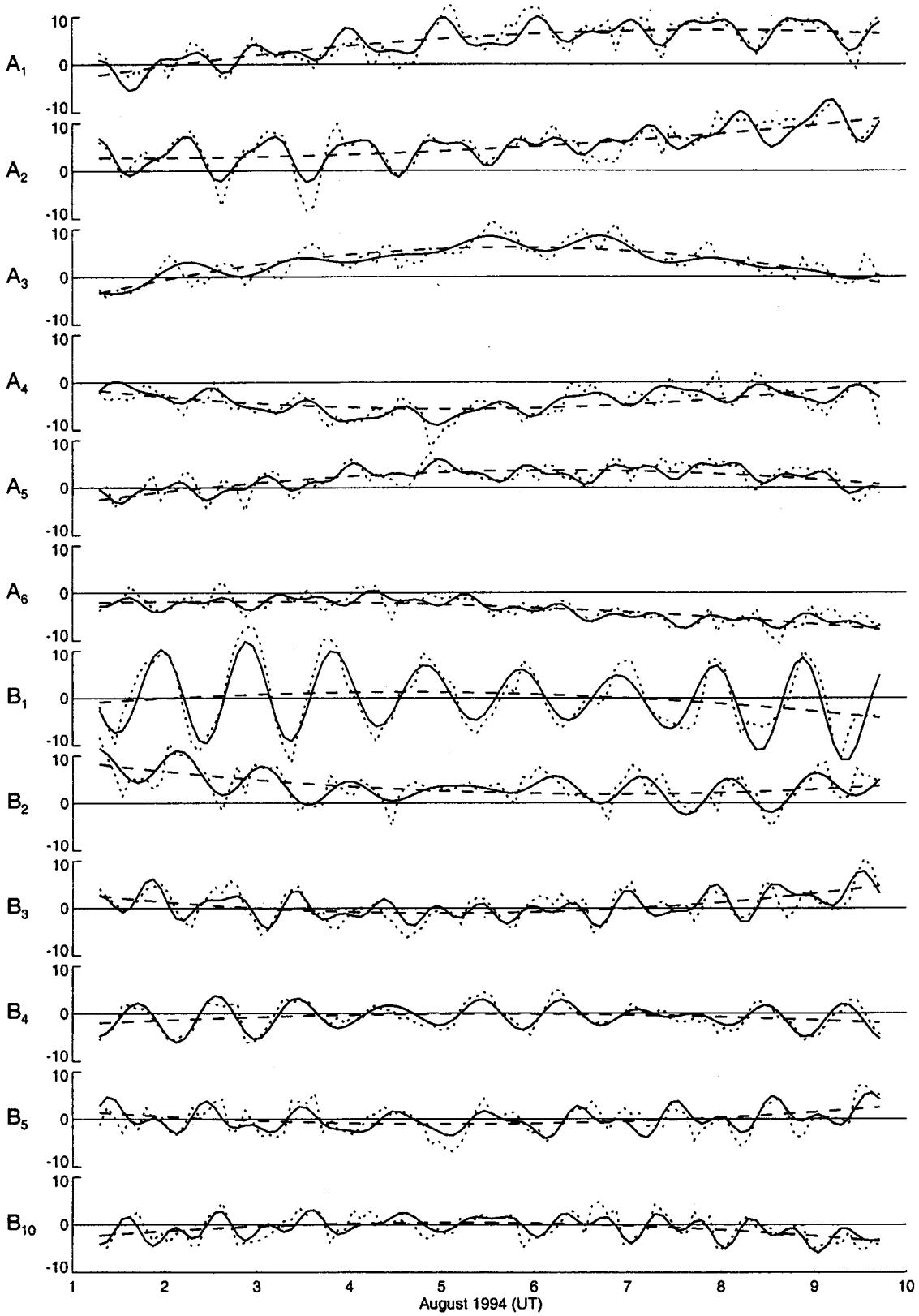

Figure 12. Time series of amplitudes A_n and B_m (in cm s^{-1}) for the spatially filtered 12-mode set. The short-dashed lines show values for the 100-mode nowcast. The solid lines show the temporally filtered values. The long-dashed lines show the quadratic fit of the 100-mode nowcast time series.

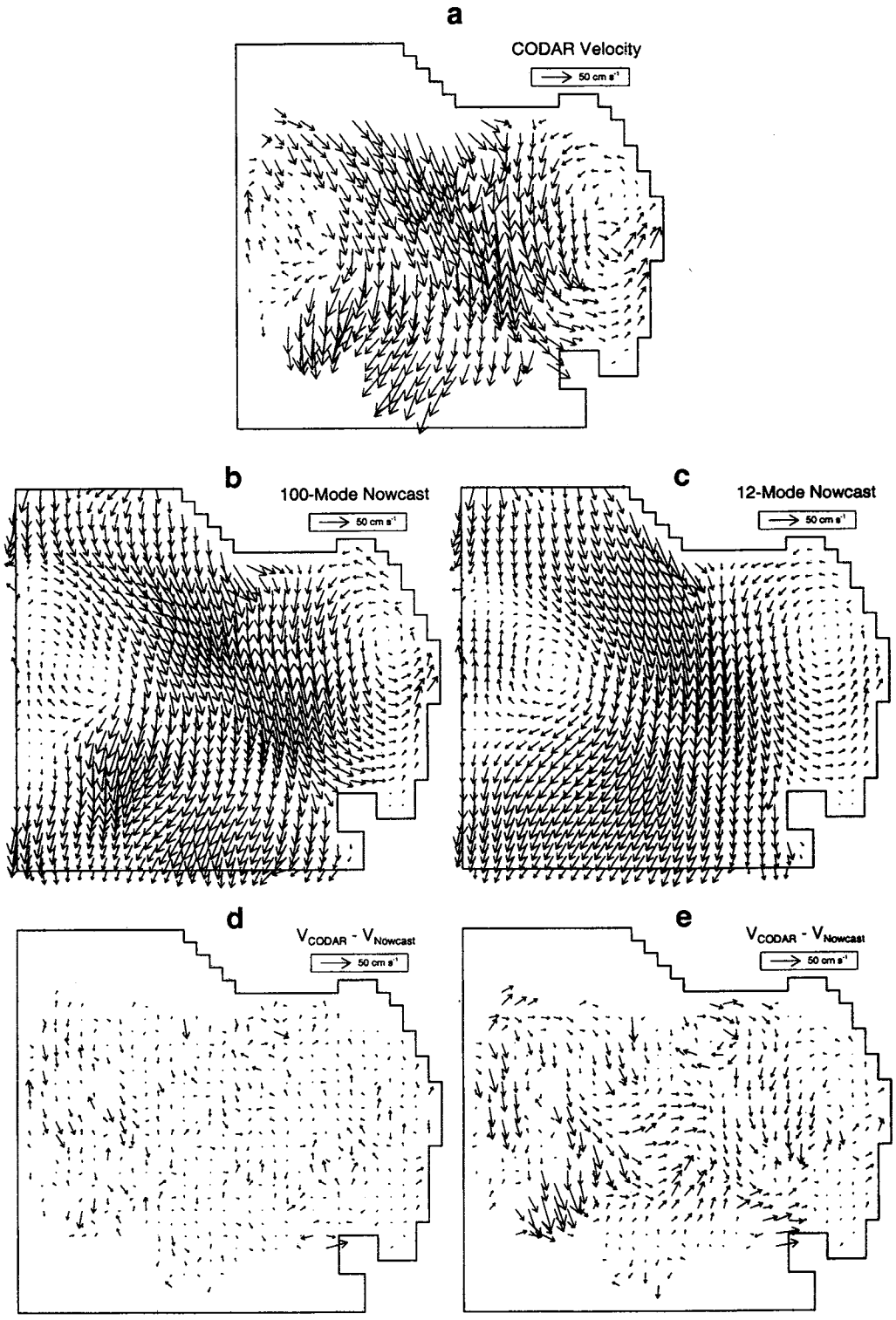

Figure 13. Comparison of 100-mode and 12-mode nowcast velocity fields for 0100 UT, August 9, 1994. The CODAR-observed velocities are shown in Figure 13a. Figure 13b shows the 100-mode nowcast velocity field. Figure 13c shows the 12-mode nowcast velocity field. Figures 13d and 13e show the difference between the CODAR and nowcast velocity fields.

noise present in the velocity measurements. As shown in (10) and (11), relative vorticity and horizontal divergence are calculated to the same order of accuracy as the velocity field using the NMA technique.

As an example, Figure 10 of *Lewis et al.* [1998] shows time series of horizontal divergence calculated from CODAR velocity observations at two adjacent grid cells, using finite differences. These time series are also shown in Figure 16a. The

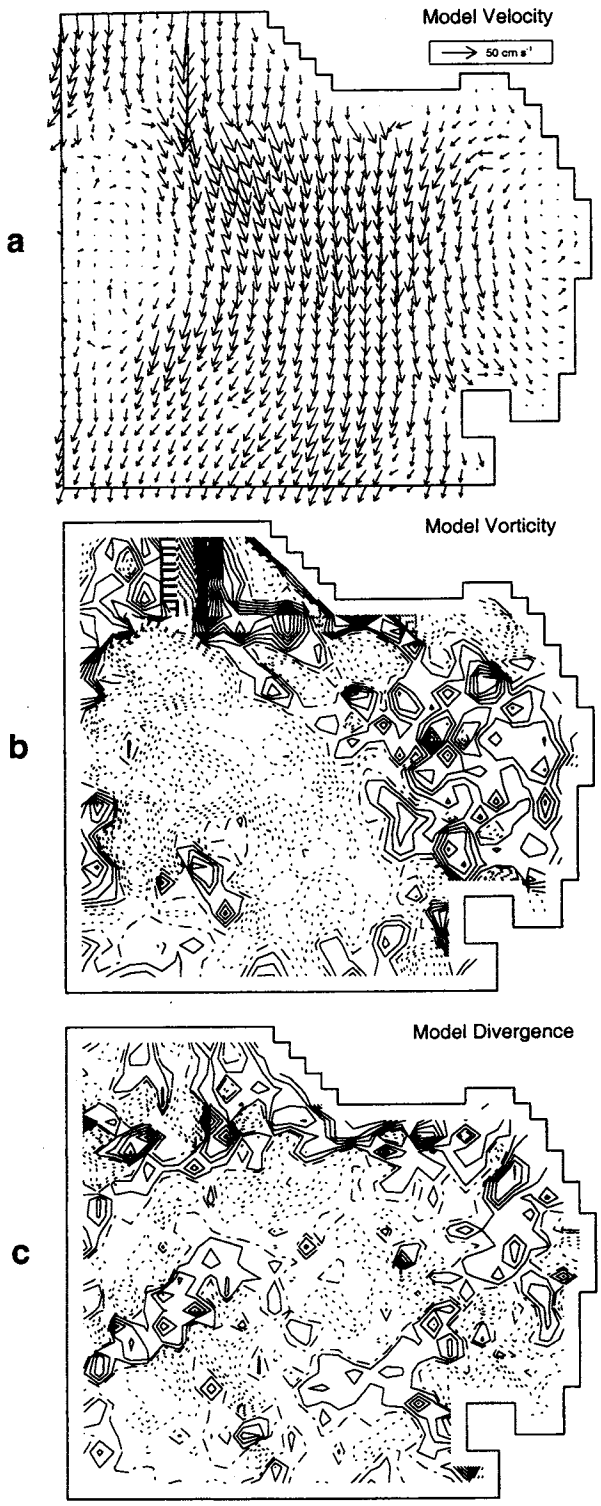

Figure 14. (a) Velocity, (b) relative vorticity, and (c) horizontal divergence from the *Lewis et al.* [1998] model at 0100 UT, August 9, 1994. For the plots of relative vorticity and divergence, solid contours show positive values, and dashed contours show negative values, with a contour interval of 1×10^{-5} s^{-1}.

two time series show large divergence fluctuations, with peak values as large as 1.6×10^{-3} s^{-1}. In addition, the divergence at these two adjacent grid cells, separated by 2.8 km, was often opposite in sign. *Lewis et al.* [1998] show that for a 2 m thick surface layer, large, oppositely signed divergence values like these over a 2 hour period will tend to produce a sea level difference between the two grid points of the order of meters. These sea level differences will generate model velocities that would act to reduce such large sea surface gradients.

Figure 16b shows the nowcast horizontal divergence at the same locations, using 100 modes. The 12-mode nowcast values are shown in Figure 16c. These results show that regardless of the number of modes used, the NMA nowcast results in a divergence field that is much more spatially coherent than the CODAR observations. The 100-mode nowcast reduces the peak divergence values by nearly a factor of 2. Spatial filtering by use of a 12-mode set reduces peak divergence values to less than one tenth of the CODAR value.

5.2. Mean Kinetic Energy

At each nowcast time, kinetic energy was calculated at all locations where CODAR velocity observations were available. The mean kinetic energy ([KE]) for all observation locations is expressed as

$$[\mathrm{KE}] = \frac{\sum_{p=1}^{P} (u_p^2 + v_p^2)}{2P}$$

where P is the total number of CODAR observations at a given time.

For the nowcast velocity fields, [KE] was calculated using nowcast velocities from the same geographic positions as the CODAR observations. Figure 17a shows a comparison of [KE] for CODAR observations, the 100-mode nowcast, and the 12-mode nowcast. From the data shown in this panel, the mean values of [KE] are 336.2 cm^2 s^{-2} for the CODAR observations, 304.5 cm^2 s^{-2} (91% of CODAR value) for the 100-mode nowcast, and 197.1 cm^2 s^{-2} (59% of CODAR value) for the 12-mode nowcast.

Figure 17b shows differences in [KE] between the CODAR observations and both the 100-mode nowcast (dashed line) and the 12-mode nowcast (dotted line). Figure 17c shows the number of CODAR velocity observations available for each time interval p.

5.3. Enstrophy

At each nowcast time, enstrophy (mean-square relative vorticity) was calculated for both the 100-mode and 12-mode nowcasts as

$$\bar{\varsigma}^2 = \frac{\iint \varsigma^2 \, dx \, dy}{\iint dx \, dy},$$

where ς is relative vorticity, defined as in (10).

Figure 18a shows time series of enstrophy for the 100-mode nowcast (solid line) and the 12-mode nowcast (long-dashed line). Figures 18b and 18c show power spectra for these two time series plots, after removing a quadratic trend from each of them. The spectrum for the 100-mode enstrophy time series is broad, with no clear spectral peaks, while the spectrum for the 12 mode case has a single dominant peak at the diurnal frequency. It is not clear why the 100-mode nowcast enstrophy contains no significant spectral peaks.

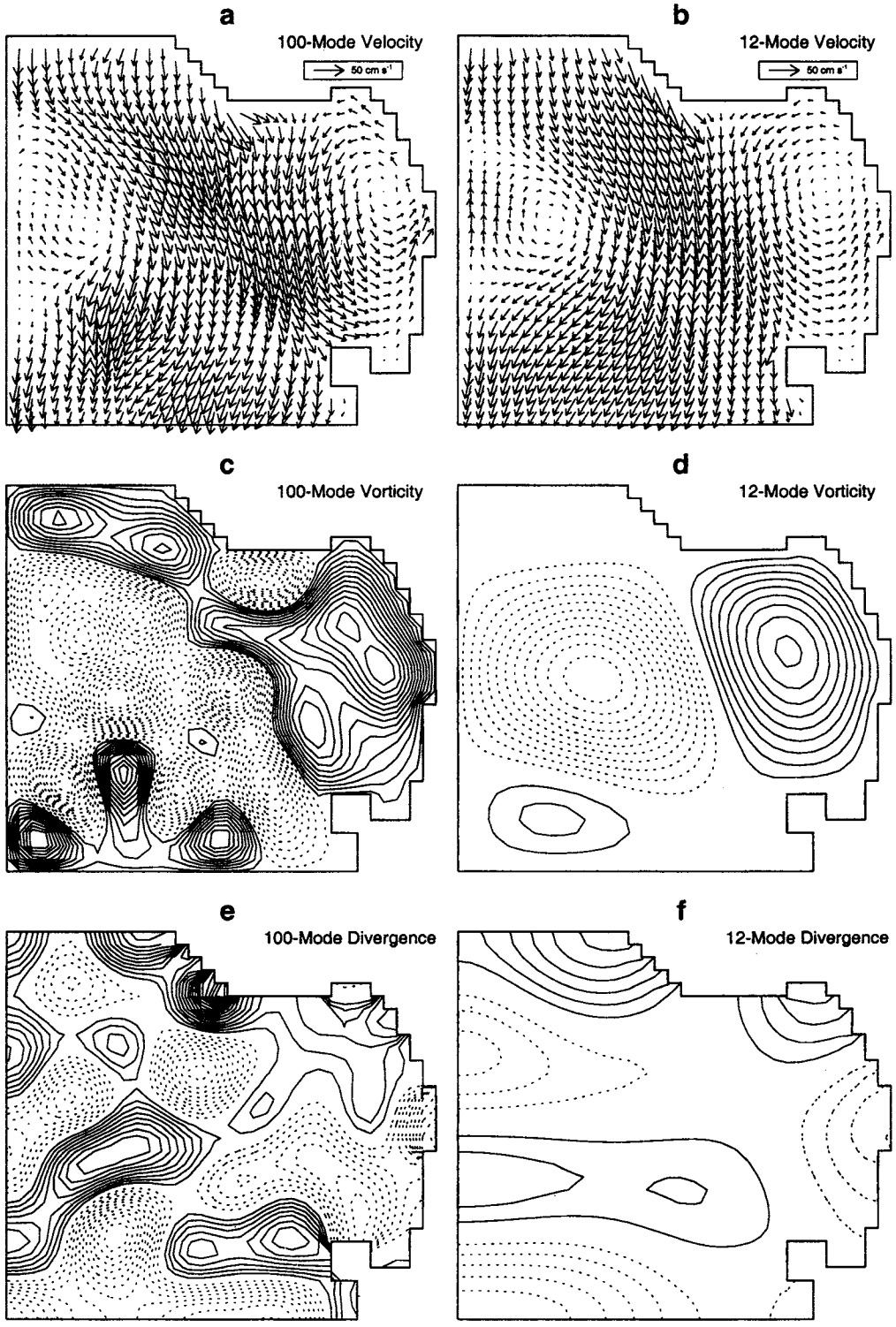

Figure 15. Comparison of 100-mode and 12-mode (a and b) nowcast velocity, (c and d) relative vorticity, and (e and f) horizontal divergence fields for 0100 UT, August 9, 1994. Figures 15a, 15c, and 15e show the 100-mode nowcast, with 12-mode nowcast results in Figures 15b, 15d, and 15f. For the plots of relative vorticity and divergence, solid contours show positive values, and dashed contours show negative values, with a contour interval of 5×10^{-6} s^{-1}.

In the absence of viscosity and sources, enstrophy is conserved in closed basins. Figure 18a shows substantial $\overline{\varsigma}^2$ fluctuations on timescales of ~4–6 hours. This is most likely caused by the presence of open boundaries. Even if the model boundary conditions did not transport vorticity into and out of the domain, the CODAR data implicitly contain fluctuations due to vorticity transport across the domain boundaries.

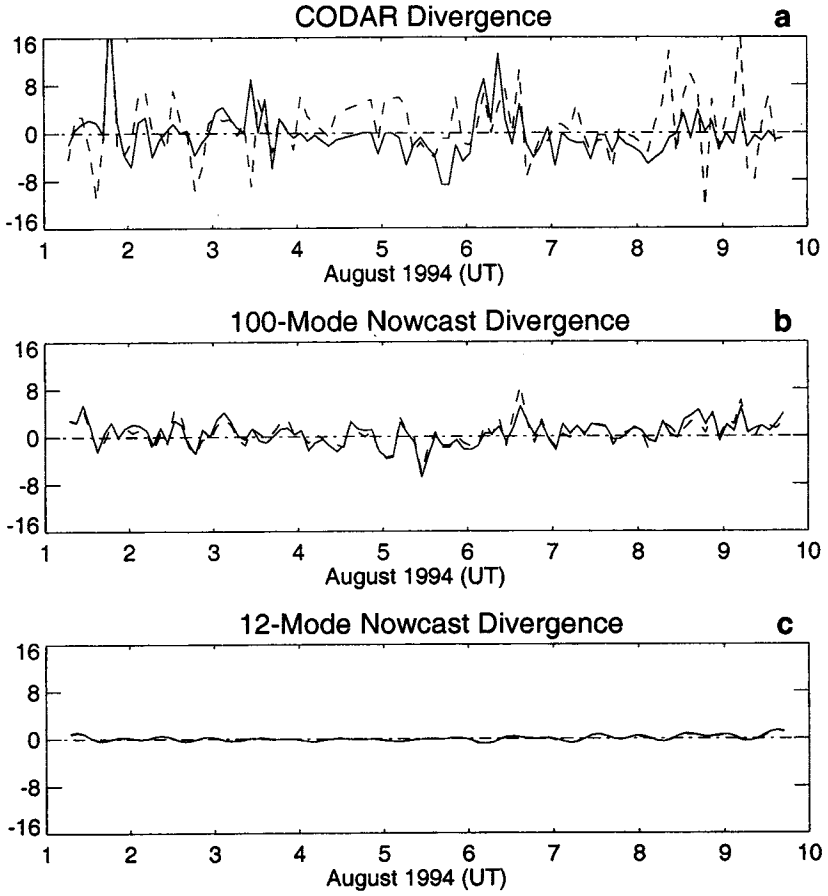

Figure 16. Time series of horizontal divergence (in 10^{-4} s^{-1}) at grid cells (20, 21) (solid lines) and (21, 20) (dashed lines) in the Monterey Bay model domain described by *Lewis et al.* [1998]. Figure 16a shows divergence calculated from CODAR observations. Figure 16b shows the 100-mode nowcast divergence. Figure 16c shows the 12-mode nowcast divergence.

5.4. Comparing the Model and Nowcasts With the CODAR Observations

Since data assimilation by the *Lewis et al.* [1998] numerical model may be viewed, by itself, as one form of nowcast, it is important to determine how the NMA nowcasts reported here offer improvement for the analysis problem. The model velocity field shown in Figure 14a agrees well with observed CODAR velocities (shown in Figure 13a). However, near the center of the northern open boundary, a line of unusually high velocities, two grid points wide and directed southward, extends to the south for 12–15 km. This line of high velocities is evident during much of the model simulation and is not readily explained, although it may be related to the optimization scheme used to calculate the open boundary conditions. As seen from Figure 1, this high-velocity line occurs over the shelf break region, so that changing bottom topography may also be causing model computational problems. On the open boundary the two high-velocity points were replaced by linearly interpolated values, using the neighboring open boundary points, prior to calculating the boundary solution used for the nowcasts described here.

Qualitatively, the CODAR-observed velocity field (Figure 13a) agrees well with the model (Figure 14a), the 100-mode nowcast (Figure 13b), and the 12-mode nowcast (Figure 13c). In order to quantify the differences between these realizations of the velocity field, root-mean-square (rms) speed differences were calculated for both the u and v velocity components as

$$(\Delta u,\ \Delta v)_{\mathrm{rms}} = \sqrt{\frac{\sum_{p=1}^{P} (u_c - \tilde{u},\ v_c - \tilde{v})^2}{P}},$$

where $(u_c,\ v_c)$ are CODAR-measured velocities, $(\tilde{u},\ \tilde{v})$ are model or nowcast velocities, and P is the total number of CODAR observations at a given time.

Figure 19 shows time series of rms speed differences for CODAR minus model (solid lines), CODAR minus 100-mode nowcast (long-dashed lines), and CODAR minus 12-mode nowcast (short-dashed lines). As a reference, the mean rms values of the measured CODAR $(u,\ v)$ are (16.1, 19.7) cm s^{-1}. The 100-mode NMA nowcast velocities are in closest agreement with the CODAR observations, with the model and 12-mode nowcast velocities showing comparable rms differences. NMA nowcasting, then, does at least as good a job as the data assimilation model in recovering the observed velocities. Note also that the peak rms speed differences between the CODAR observations and the 100-mode nowcast are comparable to the differences between CODAR and acoustic Doppler current profiler (ADCP) observations reported by *Paduan and Rosenfeld* [1996].

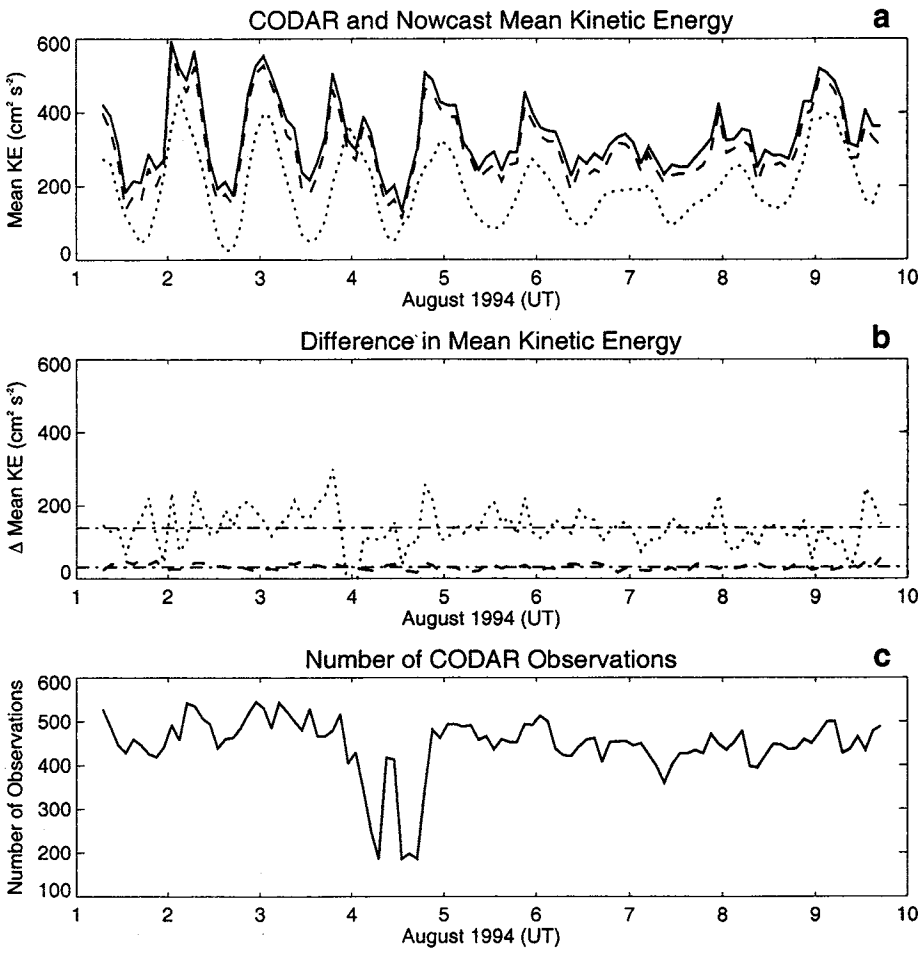

Figure 17. Time series of [KE] ($cm^2\ s^{-2}$) for (a) CODAR observations (solid line), 100-mode nowcast (dashed line), and 12-mode nowcast (dotted line). (b) Differences in [KE] between CODAR observations and the 100-mode nowcast (dashed line) and CODAR observations and the 12-mode nowcast (dotted line). (c) Number of CODAR velocity observations available for each hour. The dash-dotted lines in Figure 17b show mean values of [KE] differences.

In contrast, the model velocity gradient fields shown in Figure 14, with little spatial coherence and peak values exceeding $5 \times 10^{-5}\ s^{-1}$, differ markedly from the nowcast velocity gradient fields shown in Figure 15. NMA nowcasting, then, may be better suited to recovering the spatial structure of these gradient fields and may be an effective method for filtering these high-resolution observations prior to assimilating them into a model. Some type of filtering was suggested by *Lewis et al.* [1998] prior to data assimilation by a model, in order to reduce noise, particularly in the velocity gradient fields, and improve the model's performance.

5.5. Sensitivity to Subsampling

It is important to determine how sensitive the NMA method is to changes in the number of available CODAR velocity observations to constrain the least squares determination of the mode amplitudes. To evaluate this sensitivity, a series of nowcasts were performed, each using 50 ψ_n (Dirichlet) and 50 ϕ_m (Neumann) modes. At every time interval each CODAR observation was assigned a random number between 1 and 5. Subsampling was performed by retaining only those observations with a random number index within a specified range. For each subsampling case the number of model velocities used was held constant. Using this subsampling scheme, five nowcasts were performed, using decreasing numbers of CODAR observations.

For the first case, all available observations were used at each time interval. This case was then used as a standard for comparing the four subsequent cases, where subsampling was performed. For the four subsampled cases each A_n and B_m time series was compared with the first case to see how well the two realizations of a given amplitude agreed with each other. Agreement was measured by calculating both the correlation coefficient C and the root-mean-square difference Δ for the two amplitude time series. Using amplitude A_1 as an example, C and Δ were calculated for case 2 (A_1^2) compared with case 1 (A_1^1) as

$$C = \frac{\sum A_1^1 A_1^2}{\sqrt{\sum A_1^1 A_1^1}\sqrt{\sum A_1^2 A_1^2}},$$

$$\Delta = \sqrt{\frac{\sum (A_1^1 - A_1^2)^2}{J}}.$$

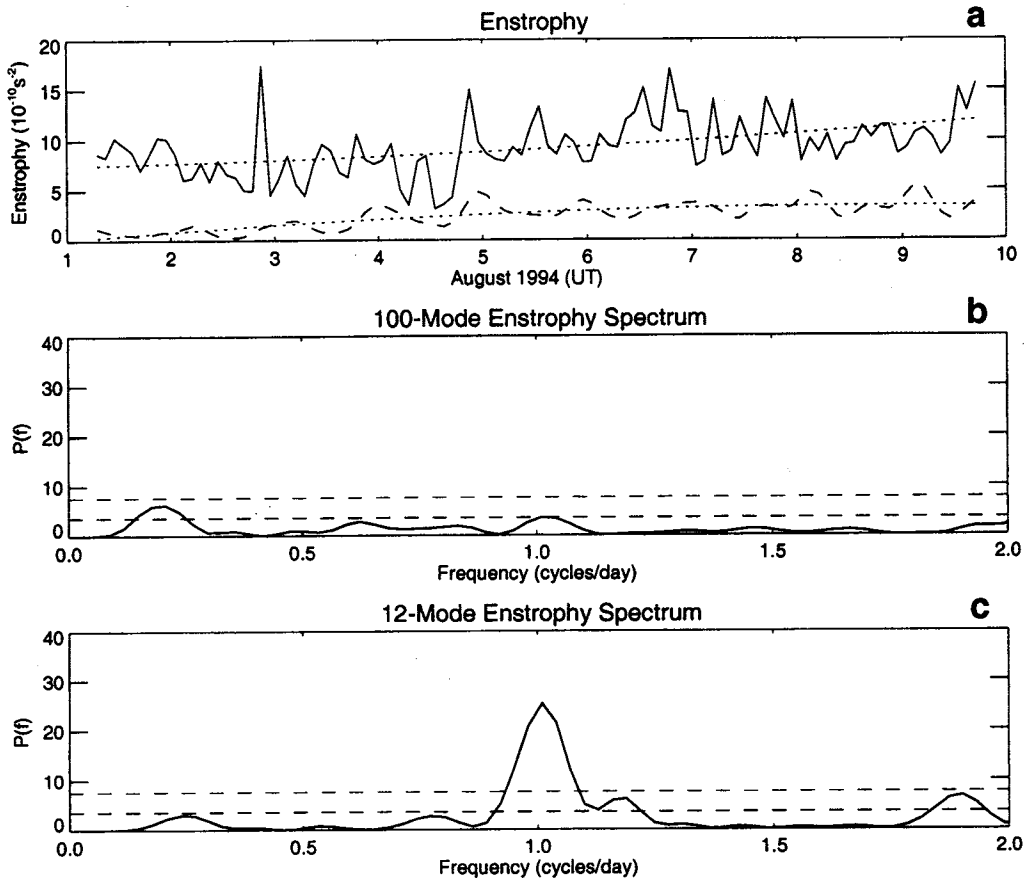

Figure 18. (a) Time series of enstrophy (10^{-10} s^{-2}) for 100-mode nowcast (solid line) and 12-mode nowcast (long-dashed line) with quadratic fits for each time series shown as short-dashed lines. (b) Power spectra for 100-mode nowcast enstrophy time series. (c) Power spectra for 12-mode nowcast enstrophy time series. The dashed lines in Figures 18b and 18c show the 5% and 95% confidence levels for the Lomb's method power spectra.

Here, the Σ symbol implies a summation over all time intervals, and J is the total number of time intervals in the time series.

A summary of the subsampling sensitivity study results is shown in Table 3. The minimum, maximum, and mean values for all 100 individual amplitude C and Δ values are shown. These results show that the NMA method is insensitive to subsampling until the number of observations is reduced to approximately the number of unknown amplitudes; that is, the system moves from overdetermined to nearly uniquely determined.

5.6. EOF Analysis of Stream Function and Velocity Potential

While the NMA basis functions provide a natural partitioning of the velocity field into vorticity and divergence components, they do not necessarily represent a compact set for describing the variance of a given field in a minimum number of modes. Empirical orthogonal functions (EOFs) are a useful tool for describing the principal variance patterns in geophysical fields in a compact way.

Complex EOFs have been used to describe the variance patterns in velocity fields. However, with the CODAR observations, some method of dealing with spatial and temporal gaps in the observations would be required. This type of analysis would yield no information about surface velocities where spatial gaps occur in the observations. Also, the EOF-reconstructed velocity field cannot be easily constrained to meet boundary flow conditions and the three-dimensional incompressibility condition.

An alternative approach is to apply EOF analysis to the NMA nowcast fields, so that the data coverage is uniform in space and time and the initial data field satisfies both the normal flow condition and three-dimensional incompressibility. The EOF-reconstructed field, then, will satisfy the open boundary flow and three-dimensional incompressibility conditions. Note that the NMA and EOF basis sets are both orthogonal, complete sets, so that they are linearly related.

Here, we take advantage of the natural partitioning of the velocity field in (1) and use scalar EOFs to examine the variance of the velocity field's two scalar components: the stream function Ψ and velocity potential Φ. Note that the Ψ field represents the vortical part of the total velocity (with zero horizontal divergence) and the Φ field represents the potential part of the total velocity (with zero relative vorticity). After subtracting the temporal mean Ψ and Φ values at each nowcast location, the 202 hour time series (at 2 hour intervals) of each of these fields were analyzed using a standard EOF technique for both the 100-mode and 12-mode nowcasts. The (100, 12)-

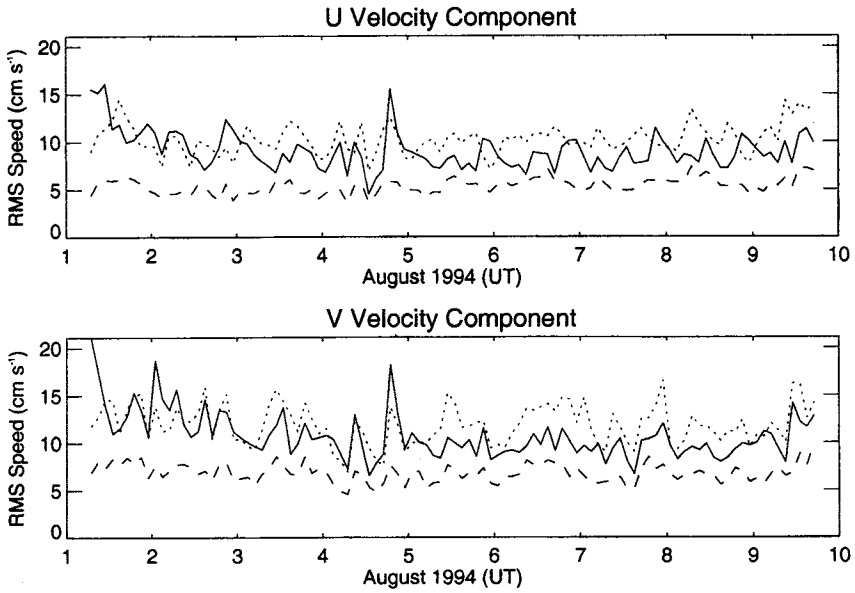

Figure 19. Time series of $(\Delta u, \Delta v)_{\text{rms}}$ in cm s^{-1} at locations where CODAR observations were made. Values are shown for CODAR minus model (solid lines), CODAR minus 100-mode nowcast (long-dashed lines), and CODAR minus 12-mode nowcast (short-dashed lines).

mode Ψ field was nowcast using (50, 6) vorticity (Dirichlet) modes, so that (50, 6) nonzero EOF eigenvalues are expected. Similarly, the (100, 12)-mode Φ field was nowcast using (50, 6) divergence (Neumann) modes, so that (50, 6) nonzero EOF eigenvalues are again expected.

Figure 20a shows the 12-mode nowcast Ψ field for 0100 UT, August 9, 1994, and Figures 20b–20e show the first four EOF modes for the 202 hour time series of this field. These four EOF modes account for 98.4% of the Ψ variance, with the first two EOF modes alone accounting for 87.3% of the variance. Figure 21 shows similar results for the 12-mode nowcast Φ field. For Φ the first four EOF modes account for 99.0% of the variance, with the first two EOF modes alone accounting for 94.6% of the variance. The percent variance explained by each EOF mode is shown at the upper right in each plot.

The percent variance explained by the first 10 EOF modes for the time series of each of these fields is shown in Table 4. Percent variance values are also shown for the EOF analysis of the 100-mode nowcast Ψ and Φ fields, for comparison. The results in Table 4 for the 12-mode nowcast Ψ field show exactly 6 nonzero EOF eigenvalues corresponding to the 6 degrees of freedom of the NMA nowcast. This is not true for the 12-mode nowcast Φ field, which includes an additional contribution from the open boundary Θ solution, as shown in (9).

The two gyres seen in the 12-mode nowcast Ψ field (Figure 20a) and apparent in the first EOF mode (Figure 20b) are quite consistent with the daily and monthly mean CODAR velocity fields reported by *Paduan and Rosenfeld* [1996]. The structure seen in the 12-mode nowcast Φ field (Figure 21a) and in the first two EOF modes for this field (Figures 21b and 21c) describes a broad irrotational flow that is generally directed toward the southeast (onshore) with some flow leaving the domain to the southwest, near the southern boundary. The time series of this Φ field shows that this flow direction changes diurnally, so that it may be viewed as describing the combined effects of wind and tidal forcing.

6. Discussion

We have demonstrated the use of a NMA technique to filter HF radar observations to produce surface velocity nowcasts. The NMA technique is capable of filtering in both space and time and provides a gap-free nowcast with relative vorticity and horizontal divergence consistent with the coastal boundary shape and any specified open boundary conditions. This type of filtering is especially well suited to the assimilation of HF radar-derived surface currents by a numerical model because the model can be used to provide open boundary flow information and interior velocity estimates in regions where large spatial gaps exist in the observations.

In one nowcast described here, a relatively large number of basis functions (100) were used to nowcast the velocity field.

Table 3. Summary of Subsampling Sensitivity Study

Case	Mean Number of Observations	C_{min}	C_{max}	C_{mean}	Δ_{min}	Δ_{max}	Δ_{mean}
1	442	...	...	...	...	...	...
2	388	0.91	1.00	0.96	0.23	0.67	0.39
3	278	0.81	1.00	0.91	0.36	1.02	0.54
4	166	0.57	1.00	0.83	0.49	1.32	0.76
5	55	0.18	0.97	0.54	0.86	3.33	1.34

C, correlation coefficient; Δ, root-mean-square difference.

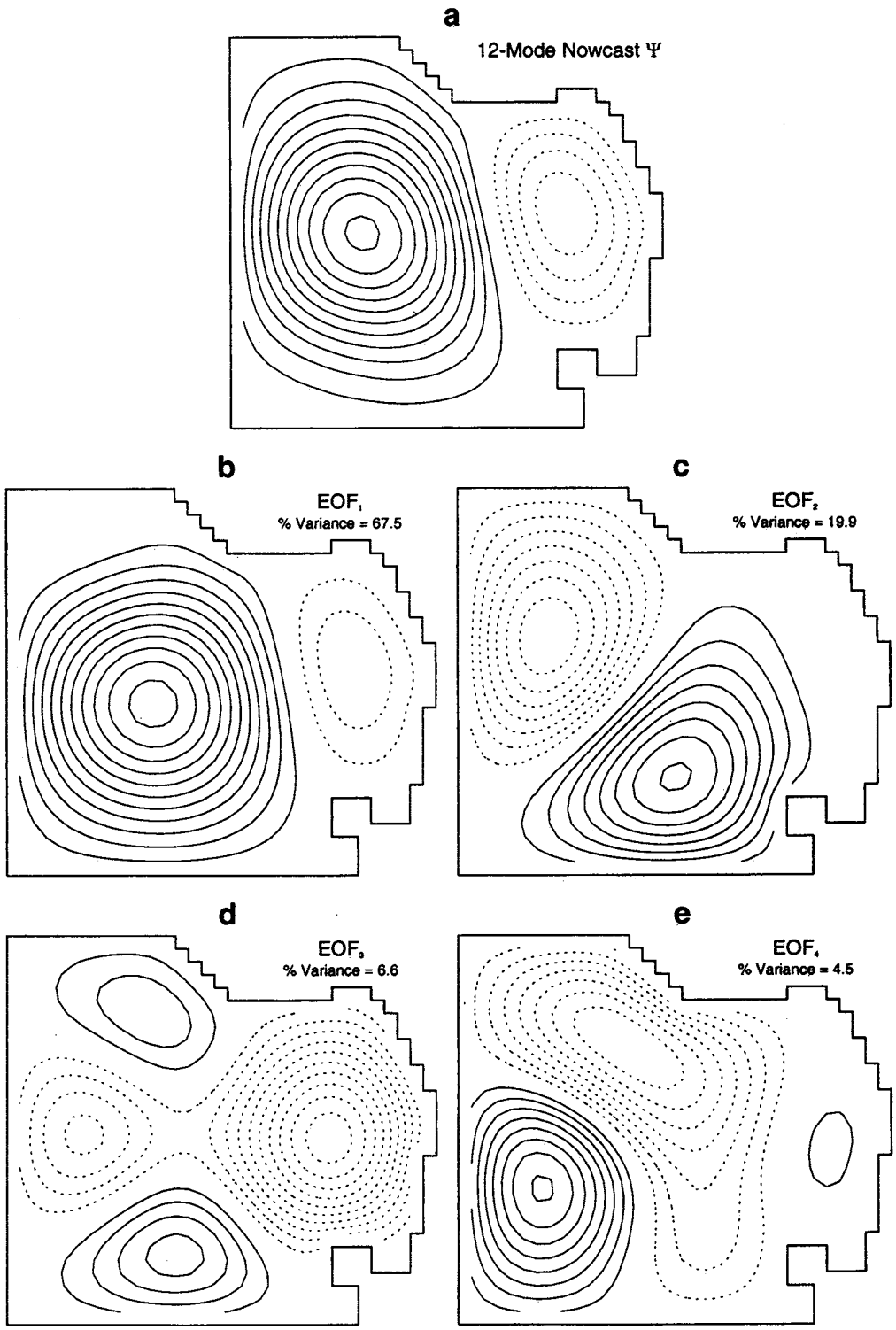

Figure 20. (a) Twelve-mode nowcast Ψ field for Monterey Bay at 0100 UT, August 9, 1994, with a contour interval of 4×10^6 cm^2 s^{-1}. (b–e) The first four empirical orthogonal function (EOF) modes for the 202 hour time series of the 12-mode nowcast Ψ field. The percent variance explained by each EOF mode is shown at the upper right in Figures 20b–20e. EOF mode contours are nondimensional. In Figures 20a–20e, positive contours are shown as solid lines, and negative contours are shown as dashed lines.

These basis functions, however, depend only on the shape of the analysis domain and do not need to be computed at each time step. For the domain shown in Figure 1, calculation of the 100 basis functions took approximately 10 min on an IBM RS6000. Once the basis functions are computed, a single nowcast computation, which might be incorporated into an ongoing data assimilation model run, requires a few seconds of clock time on the same machine.

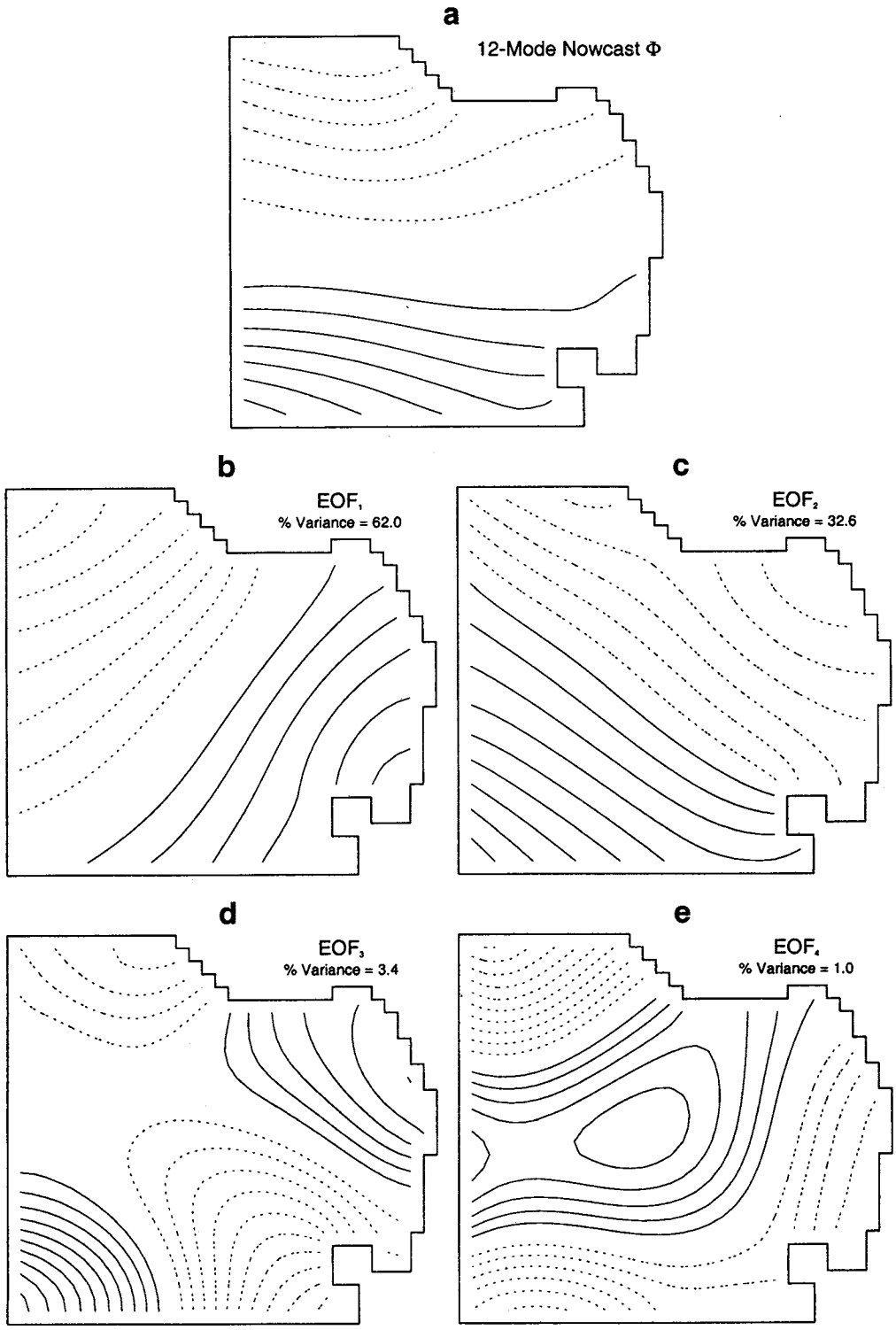

Figure 21. (a) Twelve-mode nowcast Φ field for Monterey Bay at 0100 UT, August 9, 1994, with a contour interval of 5×10^6 cm^2 s^{-1}. (b–e) The first four EOF modes for the 202 hour time series of the 12-mode nowcast Φ field. Plots and contours are shown as in Figure 20.

The analysis presented here includes an inhomogeneous solution which uses flow information at the domain's open boundaries to supplement the zero normal flow condition at the impermeable boundaries. This zero normal flow condition is satisfied automatically when the basis functions are calculated from (2) and (4). This type of constraint may not be desirable in all applications, particularly in cases where open boundary flow information is not readily available. As is obvious from section 3, the determination of the time-dependent amplitudes for the homogeneous solution does not depend on

Table 4. Percent Variance Explained by EOF Modes

EOF Mode	100-Mode Ψ	100-Mode Φ	12-Mode Ψ	12-Mode Φ
1	53.3	59.8	67.5	62.0
2	19.8	30.2	19.9	32.6
3	7.0	4.0	6.6	3.4
4	6.2	1.3	4.5	1.0
5	2.7	0.8	1.1	0.5
6	1.6	0.6	0.5	0.2
7	1.5	0.5	0.0	0.1
8	1.2	0.4	0.0	0.0
9	1.0	0.3	0.0	0.0
10	0.7	0.3	0.0	0.0
Total	95.0	98.3	100.0	100.0

EOF, empirical orthogonal function.

the presence of an inhomogeneous solution, so that the NMA nowcast technique can be applied to cases where open boundary flow is unknown.

Our first attempts at nowcasting in Monterey Bay did not use an inhomogeneous solution, so that we were modeling the Bay as a closed basin. Those early nowcasts of velocity and the velocity gradient fields were indistinguishable from those presented here at locations where CODAR observations were made. Ignoring the open boundary flow contribution, however, produced large, unrealistic flows in many of the large spatial gaps between the CODAR data footprint and the open boundaries. The inclusion of the inhomogeneous solution alleviates this problem.

Since the closed boundary nowcast is effective at locations where the observations were made, the NMA nowcast method might be very useful as a way to filter observation errors consistent with the three-dimensional incompressibility constraint. One might employ the NMA method to filter HF radar observations, for example, by extending the nowcast domain for several grid points beyond the HF radar footprint near the open boundaries. This creates a "buffer zone" where the unrealistic effects of artificially closing off these open boundaries can accumulate. The following specific points should be noted:

1. Figures 5a and 5b show that the four most energetic mode amplitudes (A_1, A_2, B_1, and B_2) have mean kinetic energy values that are >50% of the maximum value. As seen in the gradient maps for Dirichlet modes 1 and 2 in Figure 7, the two most energetic Dirichlet modes describe the vorticity structure apparent in the CODAR observations: a persistent dipole consisting of an anticyclone near the domain center and a smaller cyclone to the east, near the coast. A linear combination of these two modes resembles the dominant EOF mode structure for the Ψ field shown in Figure 20b. The gradient maps of modes 1 and 2 in Figure 9 show that the two most energetic Neumann modes describe the large-scale irrotational features apparent in the CODAR observations: diurnal cycles of broad, onshore-offshore flow attributable to the combined effects of wind and tides.

2. The scheme presented here for spatial filtering uses kinetic energy as the criterion for mode selection. Other analyses might require alternate spatial filtering schemes based on preserving variance in the Ψ, Φ, relative vorticity, or horizontal divergence fields. In addition, the cutoff value of 15% used as a criterion for spatial filtering (see Figure 5) was chosen arbitrarily. Sensitivity of the nowcast to this cutoff criterion needs to be investigated further.

3. Spectral analysis of the A_n and B_m time series (shown in Figure 10) is in itself a powerful analysis tool, since it describes oscillations in the frequency domain over the entire spatial domain, rather than at individual geographic positions.

4. The smallest spatial scales described by the modes used for the 12-mode nowcast are on the order of 20 km, a scale that greatly exceeds the CODAR resolution of 2–6 km. Since the 12-mode nowcast accounts for 59% of the CODAR-observed [KE], preserves the phase of [KE] fluctuations, and accurately describes the large-scale flow structure apparent in the CODAR observations, the surface velocity field observed by the CODAR is highly coherent over these larger scales.

5. Calculation of velocity gradient fields, including diagnostic quantities like enstrophy, is readily accomplished for any location in the domain, including the domain boundary, when the NMA basis functions are used. This is true even when the spatial footprint or spatial resolution of the observations varies with time.

6. NMA nowcasting greatly reduces observed noise while preserving spatial coherence in the relative vorticity and horizontal divergence fields. This effectively "preconditions" the CODAR observations, consistent with model boundary conditions and the constraint of three-dimensional incompressibility, so that it may be more readily assimilated into a numerical model.

7. As described in section 5.6, nowcasting with the NMA basis functions does not preclude further analysis of any kinematic field using traditional EOF methods. These methods remain a valuable tool for discovering the principal statistical patterns in these fields.

8. The numerical model boundary conditions do not include large-scale flow features such as the California Current. However, these large-scale features may be represented in the CODAR measurements. Since the CODAR data constrain the determination of A_n and B_m, large-scale flow effects, if present, are incorporated in the nowcast velocity field through these amplitudes.

9. The presence of open boundaries will continue to present a challenge for coastal ocean nowcasting. The NMA nowcasts described here rely on a primitive equation model to estimate open boundary flows. However, any source of velocity information on the open boundaries, including observations or climatology, would be sufficient to constrain the nowcast boundary problem.

10. The existence of quadratic trends in the temporally filtered A_n and B_m time series (shown in Figure 12) suggests the presence of long-period (perhaps very long period) flow variations. The periods of these motions must greatly exceed 200 hours (~10 days). Such motions are expected. The quadratic fit, then, seems to be an effective way of representing them over this short observation period.

Acknowledgments. The authors are grateful for the support of the Office of Naval Research. We thank Francisco Chavez of the Monterey Bay Aquarium Research Institute for the moored wind observations used to force our model simulations. A. D. Kirwan Jr. also acknowledges the Samuel L. and Fay M. Slover endowment to Old Dominion University. Finally, we would like to thank Jan Hesthaven from the Division of Applied Mathematics at Brown University for his insight and patience in guiding us to formulate our problem as a large, sparse matrix eigenvalue problem and for his recommendation of a reliable numerical technique for solving these problems.

References

Blumberg, A. F., and G. L. Mellor, A description of a three-dimensional coastal ocean circulation model, in *Three-Dimensional*

Coastal Ocean Models, *Coastal Estuarine Sci.*, vol. 4, edited by N. S. Heaps, pp. 1–16, AGU, Washington, D. C., 1987.

Chapman, R. D., L. K. Shay, H. C. Graber, J. B. Edson, A. Karachintsev, C. L. Trump, and D. B. Ross, On the accuracy of HF radar surface current measurements: Intercomparisons with ship-based sensors, *J. Geophys. Res.*, *102*, 18,737–18,748, 1997.

Cho, K., R. O. Reid, and W. D. Nowlin Jr., Objectively mapped stream function fields on the Texas-Louisiana shelf based on 32 months of moored current meter data, *J. Geophys. Res.*, *103*, 10,377–10,390, 1998.

Davis, R. E., Objective mapping by least-squares fitting, *J. Geophys. Res.*, *90*, 4773–4777, 1985.

Eremeev, V. N., L. M. Ivanov, and A. D. Kirwan Jr., Reconstruction of oceanic flow characteristics from quasi-Lagrangian data, 1, Approach and mathematical methods, *J. Geophys. Res.*, *97*, 9733–9742, 1992a.

Eremeev, V. N., L. M. Ivanov, A. D. Kirwan Jr., O. V. Melnichenko, S. V. Kochergin, and R. R. Stanichnaya, Reconstruction of oceanic flow characteristics from quasi-Lagrangian data, 2, Characteristics of the large-scale circulation in the Black Sea, *J. Geophys. Res.*, *97*, 9743–9753, 1992b.

Eremeev, V. N., L. M. Ivanov, A. D. Kirwan Jr., and T. M. Margolina, Amount of ^{137}Cs, and ^{134}Cs radionuclides in the Black Sea produced by the Chernobyl disaster, *J. Environ. Radioact.*, *27*, 49–63, 1995a.

Eremeev, V. N., L. M. Ivanov, A. D. Kirwan Jr., and T. M. Margolina, Analysis of the cesium pollution in the Black Sea by regularization methods, *Mar. Pollut. Bull.*, *30*, 460–462, 1995b.

Lewis, J. K., I. Shulman, and A. F. Blumberg, Assimilation of Doppler radar current data into numerical ocean models, *Cont. Shelf Res.*, *18*, 541–559, 1998.

Lipphardt, B. L., Jr., A. D. Kirwan Jr., C. E. Grosch, L. M. Ivanov, and J. K. Lewis, Merging disparate oceanographic data, paper presented at SACLANT/ONR/ODU Conference on Rapid Environmental Assessment, Lerici, Italy, 1997.

Paduan, J. D., and M. S. Cook, Mapping surface currents in Monterey Bay with CODAR-type HF radar, *Oceanography*, *10*, 49–52, 1997.

Paduan, J. D., and L. K. Rosenfeld, Remotely sensed surface currents in Monterey Bay from shore-based HF radar (Coastal Ocean Dynamics Application Radar), *J. Geophys. Res.*, *101*, 20,669–20,686, 1996.

Rao, D. B., and D. J. Schwab, A method of objective analysis for currents in a lake with application to Lake Ontario, *J. Phys. Oceanogr.*, *11*, 739–750, 1981.

Schwiderski, E. W., Global ocean tides, part V, The diurnal principal lunar tide O1, Atlas of tidal charts and maps, *NSWC Tech. Rep. 81-144*, 15 pp., Nav. Surface Weapons Cent., Silver Spring, Md., 1981.

Schwiderski, E. W., Atlas of ocean tidal charts and maps, part I, The semidiurnal principal lunar tide M2, *Mar. Geod.*, *6*, 219–265, 1983.

C. E. Grosch, Center for Coastal Physical Oceanography, Old Dominion University, 768 West 52nd Street, Norfolk, VA 23529.

A. D. Kirwan and B. L. Lipphardt, College of Marine Studies, University of Delaware, Robinson Hall, Newark, DE 19716. (adk@udel.edu; brucel@udel.edu)

J. K. Lewis, Ocean Physics Research & Development, P. O. Box 1029, Kalaheo, HI 96741. (ocnphys@aloha.net)

J. D. Paduan, Department of Oceanography, Naval Postgraduate School, 833 Dyer Road, Room 328, Monterey, CA 93942. (paduan@oc.nps.navy.mil)

(Received January 19, 1999; revised September 14, 1999;
accepted October 21, 1999.)